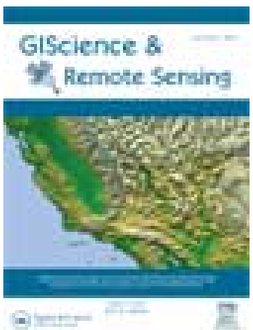

GIScience & Remote Sensing

ISSN: (Print) (Online) Journal homepage: https://www.tandfonline.com/loi/tgrs20

Peatland leaf-area index and biomass estimation with ultra-high resolution remote sensing

Aleksi Räsänen , Sari Juutinen , Margaret Kalacska , Mika Aurela , Pauli Heikkinen , Kari Mäenpää , Aleksi Rimali & Tarmo Virtanen

To cite this article: Aleksi Räsänen , Sari Juutinen , Margaret Kalacska , Mika Aurela , Pauli Heikkinen , Kari Mäenpää , Aleksi Rimali & Tarmo Virtanen (2020): Peatland leaf-area index and biomass estimation with ultra-high resolution remote sensing, GIScience & Remote Sensing

To link to this article: https://doi.org/10.1080/15481603.2020.1829377

GISCIENCE & REMOTE SENSING
https://doi.org/10.1080/15481603.2020.1829377

Taylor & Francis
Taylor & Francis Group

Peatland leaf-area index and biomass estimation with ultra-high resolution remote sensing

Aleksi Räsänen[a], Sari Juutinen[a,b], Margaret Kalacska[c], Mika Aurela[b], Pauli Heikkinen[d], Kari Mäenpää[d], Aleksi Rimali[d] and Tarmo Virtanen[a]

[a]Ecosystems and Environment Research Programme, Faculty of Biological and Environmental Sciences, and Helsinki Institute of Sustainability Science (HELSUS), University of Helsinki, Helsinki, Finland; [b]Climate System Research, Finnish Meteorological Institute, Helsinki, Finland; [c]Department of Geography, McGill University, Montreal, Canada; [d]Space and Earth Observation Centre, Finnish Meteorological Institute, Sodankylä, Finland

ABSTRACT

There is fine-scale spatial heterogeneity in key vegetation properties including leaf-area index (LAI) and biomass in treeless northern peatlands, and hyperspectral drone data with high spatial and spectral resolution could detect the spatial patterns with high accuracy. However, the advantage of hyperspectral drone data has not been tested in a multi-source remote sensing approach (i.e. inclusion of multiple different remote sensing datatypes); and overall, sub-meter-level leaf-area index (LAI) and biomass maps have largely been absent. We evaluated the detectability of LAI and biomass patterns at a northern boreal fen (Halssiaapa) in northern Finland with multi-temporal and multi-source remote sensing data and assessed the benefit of hyperspectral drone data. We measured vascular plant percentage cover and height as well as moss cover in 140 field plots and connected the structural information to measured aboveground vascular LAI and biomass and moss biomass with linear regressions. We predicted both total and plant functional type (PFT) specific LAI and biomass patterns with random forests regressions with predictors including RGB and hyperspectral drone (28 bands in a spectral range of 500–900 nm), aerial and satellite imagery as well as topography and vegetation height information derived from structure-from-motion drone photogrammetry and aerial lidar data. The modeling performance was between moderate and good for total LAI and biomass (mean explained variance between 49.8 and 66.5%) and variable for PFTs (0.3–61.6%). Hyperspectral data increased model performance in most of the regressions, usually relatively little, but in some of the regressions, the inclusion of hyperspectral data even decreased model performance (change in mean explained variance between −14.5 and 9.1%-points). The most important features in regressions included drone topography, vegetation height, hyperspectral and RGB features. The spatial patterns and landscape estimates of LAI and biomass were quite similar in regressions with or without hyperspectral data, in particular for moss and total biomass. The results suggest that the fine-scale spatial patterns of peatland LAI and biomass can be detected with multi-source remote sensing data, vegetation mapping should include both spectral and topographic predictors at sub-meter-level spatial resolution and that hyperspectral imagery gives only slight benefits.

ARTICLE HISTORY
Received 13 May 2020
Accepted 22 September 2020

Keywords
Biomass; hyperspectral imaging; leaf-area index; ultra-high spatial resolution; unmanned aerial systems (UAS)

Introduction

Leaf-area index (LAI) and biomass are among the most important vegetation properties linked to biogeochemical processes (Wilson et al. 2007; van der Wal and Stien 2014). Green LAI quantifies the photosynthesizing leaf area per unit ground area and thus characterizes the interface between vegetation and atmosphere. It is a key parameter when the eddy covariance or chamber-based measurements of CO_2 and CH_4 are upscaled or modeled (Tuovinen et al. 2019; Wilson et al. 2007; Metzger et al. 2015). Plant biomass, in turn, refers to total mass of plants; thus, it quantifies carbon stock in the vegetation and is closely linked to ecosystem productivity (Epstein et al. 2012; van der Wal and Stien 2014).

One way to characterize qualitative differences in vegetation is to assess LAI and biomass of different plant functional types (PFTs) (Juutinen et al. 2017; Yu et al. 2017). PFTs form a way to divide plant species into groups based on their growth forms and environmental responses (Duckworth, Kent, and Ramsay 2000; Ustin and Gamon 2010; Chapin et al. 1996). Users and their needs define the PFT grouping, but a common approach is to use groups such as evergreen and

CONTACT Aleksi Räsänen aleksi.rasanen@helsinki.fi
Supplemental data for this article can be accessed here.

deciduous shrubs, forbs, graminoids, and different types of mosses (Hugelius et al. 2011; Chapin et al. 1996; Räsänen et al. 2019). These PFTs differ in terms of how LAI and biomass are connected to plant percentage cover and height (Räsänen et al. 2019).

To capture the spatial patterns of LAI and biomass, remote sensing-based maps have been used for decades (Laidler and Treitz 2003; Walker et al. 2003). These maps can be PFT-specific (Greaves et al. 2016; Myers-Smith et al. 2015) or summed estimates of total LAI or biomass (Räsänen et al. 2019; Berner et al. 2018). Within treeless northern boreal or arctic environments, such as peatlands and tundra, the landscape is characterized by fine-scale spatial heterogeneity, controlled by variation in soil and bedrock characteristics, topography, and moisture. In particular, northern peatlands are usually flat but have notable heterogeneity in microtopography and vegetation evidenced by contrasting microforms, which often include wet and low-lying flarks, intermediate lawns and dry strings located higher than the other microforms (Laitinen et al. 2007). In these landscapes, ultra-high to very-high spatial resolution remote sensing datasets should be used (Virtanen and Ek 2014; Palace et al. 2018; Räsänen and Virtanen 2019), as the use of coarser-resolution maps can lead to erroneous landscape-level estimates of vegetation properties and associated biogeochemical processes (Räsänen and Virtanen 2019; Treat et al. 2018). Nevertheless, sub-meter-level LAI and biomass maps have rarely been developed for peatland landscapes, though such maps have been constructed in other environments such as temperate dryland (Cunliffe, Brazier, and Anderson 2016), shrub-dominated tundra (Cunliffe et al. 2020) and in particular in agricultural areas (Li et al. 2020; Yue et al. 2017; Poley and McDermid 2020).

In practice, ultra-high-resolution data can be gathered with unmanned aerial vehicles (i.e. drones). It also has been shown that there are multiple benefits when multi-source data is used, i.e. inclusion of multiple different datatypes collected from multiple different platforms, such as the combination of optical imagery and lidar data. In particular, with multi-source data, different aspects of the landscape, such as spectral, topographic, and vegetation height properties at multiple spatial resolutions can be captured. Thereby, the explanatory capacities are typically higher than when using a single data source (Räsänen and Virtanen 2019; Chen, Huang, and Xu 2017; Arroyo-Mora et al. 2017; Luo et al. 2016; Sankey et al. 2018; Poley and McDermid 2020), and further boosts in model performance can be obtained with multi-temporal data (Halabisky, Babcock, and Moskal 2018; Gholizadeh et al. 2020; Poley and McDermid 2020).

Although there are multiple different potential data sources, it has been discussed that some data such as hyperspectral imaging have multiple benefits as it can capture finer spectral signatures of vegetation than multispectral sensors (Chen, Chen, et al. 2017; Cole, McMorrow, and Evans 2013; Harris, Charnock, and Lucas 2015; Kalacska, Lalonde, and Moore 2015). In peatland landscapes, it has been shown that multiple vegetation properties can be tracked with hyperspectral data, for instance, floristic gradients (Harris, Charnock, and Lucas 2015), biotopes (Middleton et al. 2012), PFTs (Cole, McMorrow, and Evans 2013), and plant strategy types or plant traits (Kattenborn et al. 2017; Schmidtlein et al. 2012), including nitrogen and chlorophyll content (Kalacska, Lalonde, and Moore 2015). In spatially heterogeneous landscapes, the benefits of hyperspectral imaging are in particular evident with drone-based data, which can quantify the spectral properties of vegetation in high spatial and spectral resolutions (Aasen and Bolten 2018; Arroyo-Mora et al. 2019; Sankey et al. 2018; Aasen et al. 2015). However, relatively few studies have analyzed the advantages of hyperspectral drone data relative to other datasets in analyzing vegetation patterns in peatlands.

We address two major gaps in scientific knowledge, i.e. the lack of ultra-high-resolution LAI and biomass maps and the lack of testing the relative importance of hyperspectral drone data to map vegetation patterns in northern peatlands. We use multi-source and multi-temporal ultra-high-resolution remote sensing data to predict LAI and aboveground biomass patterns in a northern boreal fen landscape located in northern Finland. We ask the following two research questions. (1) How well can LAI and biomass patterns be detected with multi-source and multi-temporal ultra-high spatial resolution remote sensing data? (2) What is the benefit of hyperspectral drone data?

Materials and methods

Study area

Our study area is located in Halssiaapa fen in Sodankylä, northern Finland Figure 1. The fen has

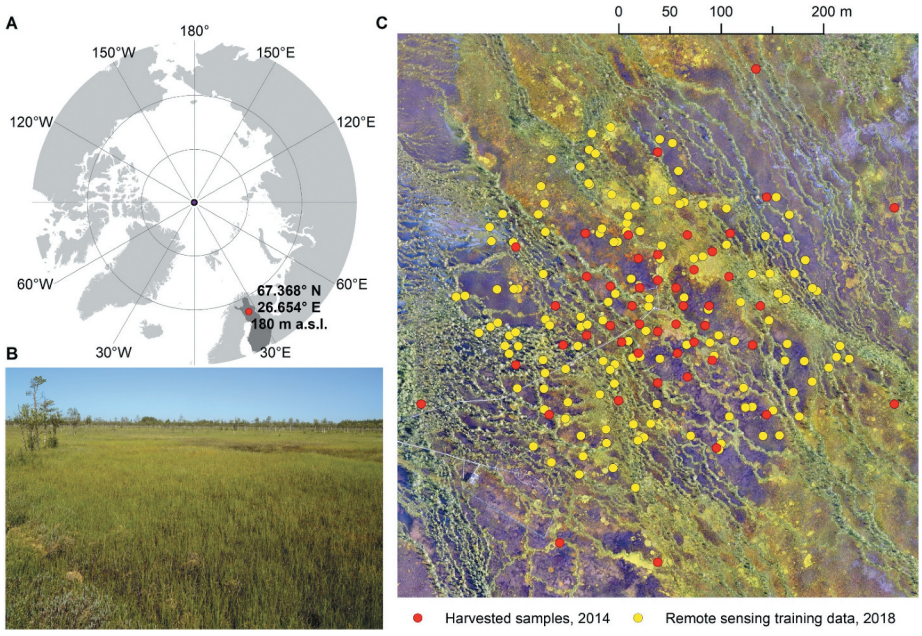

Figure 1. A) The location of study area in northern Finland, B) a photo from the study area, C) true-color drone image taken on 12 July 2016 with field inventory plots marked with dots.

fine-scale variation in vegetation, topography, wetness, and trophic status patterns (Dinsmore et al. 2017; Räsänen et al. 2019). The spatial heterogeneity can be characterized by three microforms: relatively low and dry strings (<0.5 m height) dominated by *Sphagnum* and evergreen and deciduous shrubs (e.g. *Andromeda polifolia* and *Betula nana*) and scattered birches (*Betula pubescens*) and pines (*Pinus sylvestris*); wetter flarks dominated by wet brown mosses (e.g. *Scorpidium* spp, *Warnstorfia exannulata*) and some graminoids (e.g. *Carex limosa and Eriophorum rufescens*); and intermediate lawns with continuous *Sphagnum* cover, forbs (e.g. *Menyanthes trifoliata, Comarum palustre*), graminoids (e.g. *Scheuchzeria palustris*) and some shrubs (e.g. *Vaccinium oxycoccos*). Trophic status varies from oligotrophic to eutrophic, and the transitions between different vegetation types and microforms are relatively gradual.

Vegetation inventories

To collect ground and field layer LAI and aboveground biomass vegetation inventory data, we harvested samples from 48 square plots with 50 cm side length on July 17–19, 2014 Figure 1. Species were classified into the following PFTs: evergreen dwarf shrubs, deciduous dwarf shrubs, forbs, graminoids, *Sphagnum* and other mosses. The PFT classification we used was a slight modification of the one presented by Chapin et al. (1996). The plots were located along 250 m long transects to the cardinal, intercardinal, and secondary intercardinal directions from an eddy covariance flux tower located in the fen. We selected the plots so that all major land cover and vegetation types within the fen were included. We estimated the percentage cover of each PFT visually and measured the mean height of vascular plant PFTs using a ruler. We harvested aboveground parts of the plant species to measure LAI for vascular plants and biomass for vascular plants and mosses. We collected all the aboveground vascular plant material. For mosses, we collected a 5 cm x 5 cm sample of living green photosynthesizing part of the mosses. For measuring vascular LAI, we scanned the species or PFT-specific harvested samples with an A4 scanner and processed the scans with GIMP 2.8. software (The GIMP team, www.gimp.org). From each scanned image, we calculated the proportion of green pixels. For determining biomass, we oven dried the samples at 60°C for 24 hours (Klein and Bay 1994) and weighed them.

To collect training data for remote sensing-based regressions of LAI and biomass, we sampled 140 square plots with 50 cm side length using stratified random sampling on July 17–21, 2018 Figure 1. Strata were four different land cover types from a multi-source remote sensing-based land cover map

(Mikola et al. manuscript in preparation). The plots were located at least 3 m apart from each other and the exact positions of the plots were collected with a Trimble R10 GPS device with ±5 cm accuracy. At each plot, we evaluated the cover of vascular plant and moss species with visual interpretation and measured the mean height of vascular plant species with a ruler. To ensure the consistency in visual estimation of percentage cover, the last author inventoried part of the vegetation plots and trained the other surveyors during both field campaigns. Although there were some trees in the landscape, no trees were located in our field inventory plots; thus, we excluded trees (height >1.5 m) in our analysis.

Remote sensing datasets

The use of multi-source and multi-temporal remote sensing data has been documented to increase model performance in vegetation mapping, including biomass and LAI estimation (Halabisky, Babcock, and Moskal 2018; Chen, Huang, and Xu 2017; Sankey et al. 2018; Poley and McDermid 2020; Michez et al. 2018). Furthermore, it has been shown that optimal timing of remote sensing data depends on the studied ecosystem and target variable (Cole, McMorrow, and Evans 2014; Basnyat et al. 2004; Wang et al. 2019). Therefore, we used remote sensing data depicting the spectral, topography, and vegetation height properties captured from drone, aerial, and satellite platforms with 0.02-m to 3-m spatial resolution from multiple years and phenological stages (Table 1). In total, we calculated 359 features for each of the 140 field inventory plots. We calculated the mean value of each of the layers we used; in addition, we calculated the coefficient of variation for each hyperspectral band as well as a mean coefficient of variation over all bands (Wang et al. 2018).

We used hyperspectral drone images from two time points, one from the peak growing season (July 2019) and one from the beginning of senescence (late August 2019) Table 1, Figure 2. We acquired the imagery with the Senop Rikola (Senop Oy, Oulu, Finland) frame-based snapshot camera (1010 × 1010 pixels with 36.5° field of view) mounted on a DJI Matrice 600 hexacopter. We covered a 20 ha area with a 35–40 min flight time (11:10–11:45 AM on Jul 24, and 12:00–12:40 PM on Aug 28) at an altitude of 100 m and speed of 15 km h^{-1} (4.2 m s^{-1}) resulting in ca. 1700 frames at 7 cm spatial resolution. The imagery was composed of 28 bands spanning the spectral range of 500–900 nm with an average bandwidth (full-width at half-maximum) of 8.9 nm (Table S1, Figure 2). We first converted the raw image data into radiance and applied a lens correction with the Rikola preprocessing software (Senop Oy, Oulu, Finland). As all the hyperspectral bands were acquired separately, the bands were not perfectly aligned and needed to be co-registered (Honkavaara et al. 2017; Jakob, Zimmermann, and Gloaguen 2017). We used the scale-invariant feature transform algorithm implemented in the MEPHySTo software for a practically perfect co-registration of the bands (Jakob, Zimmermann, and Gloaguen 2017). Then, we converted the images into reflectance and constructed mosaics with structure-from-motion (SfM) photogrammetry (Aasen et al. 2015) in Agisoft Metashape (Agisoft LLC, St. Petersburg, Russia). We conducted the reflectance conversion with empirical line calibration by utilizing three squared MosaicMill reflectance plates (MosaicMill Oy, Vantaa, Finland) with 0.5 m side length in 9%, 44%, and 75% reflectance. The plates were photographed during the flights. We georeferenced the image mosaics with 15 ground control points geolocated with a Trimble R10 GPS device with ±5 cm accuracy. In addition to spectral bands, we calculated 80 different vegetation indices Table 2 with the hsdar package in R (Lehnert et al. 2019).

In addition to the hyperspectral imagery, we used true-color drone images from two time points, from a wetter (2016) and a drier year (2018) Table 1, Fig. S1. We acquired the images with a DJI Phantom 4 Pro (4000 × 3000 pixels with 70°/50° field of view) and processed the data using SfM photogrammetry (Kalacska et al. 2017) in Pix4D (Pix4D S.A., Lausanne, Switzerland). On one hand, it has been shown that vegetation structure information is important in predicting biomass and LAI patterns (Poley and McDermid 2020; Cunliffe, Brazier, and Anderson 2016); on the other hand, peatland vegetation is largely controlled by micro-topographical variation (Räsänen and Virtanen 2019; Lehmann et al. 2016). Therefore, we produced 2-cm spatial resolution orthomosaics as well as a 9-cm spatial resolution digital terrain model (DTM) and vegetation height model (DTM subtracted from a digital surface model) Table 1. We georeferenced the 2018 image with 15 ground control points and co-registered the

Table 1. Remote sensing features used in leaf-area index and biomass regressions. Hyperspectral drone features are listed in Tables 2 and S1.

Dataset	Date	Producer	Spatial resolution	Number and list of layers
Hyperspectral drone images	24 July 2019; 28 August 2019	Authors	0.07 m	274: 28 bands, 80 indices, 29 coefficient of variation measures for both images
Drone image 1	12 July 2016	Authors	0.02 m	27: B, G, R, and 8 GLCM layers from all spectral bands
Drone image 2	11 July 2018	Authors	0.02 m	3: B, G, R
Drone digital elevation and terrain model	11 July 2018	Authors	0.09 m	6: Elevation, slope, TPIs (2 m and 5 m distance), TWI, VHM
Aerial image	19 August 2015	National Land Survey of Finland	0.5 m	4: B, G, R, NIR
Lidar data	19 August 2015	National Land Survey of Finland	0.5 points m^{-2} (point cloud); 2 m (layers)	9: Elevation, slope, TPIs (5 m, 10 m, 20 m, 50 m, 100 m distances), TWI, VHM
PlanetScope images	May 16, Jun 2, Jun 17, Jul 3, Jul 10, Jul 19, Jul 27, Aug 8, Aug 26, Sep 9, Sep 18, 4 October 2018	Planet Labs Inc.	3 m	36: NDVI, NDWI, RGI from all images

Abbreviations: B, blue; G, green; GLCM, gray-level co-occurrence matrix; NDVI, normalized difference vegetation index; NDWI, normalized difference water index; NIR, near-infrared; R, red; RGI, red-green index; TPI, topographical position index; TWI, topographical wetness index; VHM, vegetation height model.

2016 image with the 2018 image using 20 control points.

In previous studies, it has been discussed that some of the LAI, biomass, and other vegetation patterns can be best detected with coarser resolution data (Poley and McDermid 2020; Räsänen et al. 2020). To detect coarser spatial resolution patterns of vegetation and topography, we included aerial lidar data and orthophotos. From the lidar data, we used a 2-m resolution DTM preprocessed by the National Land Survey and computed a vegetation height model by subtracting the DTM from a digital surface model in which we used all returns of the lidar point cloud. As vegetation spectral responses vary throughout the phenological cycle in peatlands (Cole, McMorrow, and Evans 2014), we used the surface reflectance product of 12 PlanetScope satellite images (Planet Team) taken between mid-May and early October 2018 Table 1.

Textural features have been shown to boost the accuracy in remote sensing-based mapping tasks (Mishra et al. 2018; Hall-Beyer 2017). Thus, for each spectral band of the 2016 drone image, we calculated eight gray-level co-occurrence matrix (GLCM) textural features (energy, entropy, correlation, inverse difference moment, inertia, cluster shade, cluster prominence and Haralick correlation) (Haralick, Dinstein, and Shanmugam 1973) with a moving window technique, eight quantization levels and neighborhood distance set to five in Orfeo Toolbox (Grizonnet et al. 2017). We computed the following topographical features from the drone and lidar-based DTM: elevation, slope in degree, position index with different neighborhood radiuses (Guisan, Weiss, and Weiss 1999), and wetness index (Böhner and Selige 2006) in the SAGA GIS (Conrad et al. 2015). Instead of using the spectral bands as such for the PlanetScope images, we calculated the following band indices for each image: normalized difference vegetation index (NDVI) (Rouse et al. 1974), normalized difference water index (NDWI) (McFeeters 1996), and red-green index (RGI) (Coops et al. 2006) for each image Table 1.

Data analysis

First, we established empirical relationships between (1) field-measured plant species cover and height, and (2) LAI and biomass for different PFTs using the harvested samples from 2014. We tested linear regressions with the following explanatory variable options: cover only and plant volume (cover × height), compared the performance of the two models and chose the final model based on root mean squared error (RMSE) value. We evaluated the final model performance with RMSE, normalized RMSE (nRMSE: i.e., RMSE divided by the difference between maximum observed value and minimum observed value), and adjusted coefficient of determination. We used the equations from linear regressions to predict PFT-specific LAI and biomass values for vegetation plots inventoried in 2018.

Second, for predicting LAI and biomass with remote sensing datasets, we conducted random

Table 2. Details of the high spectral resolution vegetation indices calculated for the hyperspectral data. In the equations, R refers to reflectance at a specific wavelength and D to first derivation of reflectance values at the wavelength.

Index	Equation	Reference
Boochs	D_{703}	Boochs et al. (1990)
Boochs2	D_{720}	Boochs et al. (1990)
CARI*	$R_{700}\times\lvert a \times 670 + R_{670} + b\rvert/R_{670}\times(a^2 + 1)^{0.5}$	Kim et al. (1994)
Carter2	R_{695}/R_{760}	Carter (1994)
Carter3	R_{605}/R_{760}	Carter (1994)
Carter4	R_{710}/R_{760}	Carter (1994)
Carter5	R_{695}/R_{670}	Carter (1994)
Carter6	R_{550}	Carter (1994)
CI	$R_{675}\times R_{690}/R_{683}^{2}$	Zarco-Tejada et al. (2003)
CI2	$R_{760}/R_{700}-1$	Gitelson, Gritz, and Merzlyak (2003)
CIAInt	$\frac{R_{735}}{R_i}$	Oppelt and Mauser (2004)
	$\frac{R_{600}}{}$	
CRI1	R_{515}^{-1}-R_{550}^{-1}	Gitelson, Gritz, and Merzlyak (2003)
CRI2	R_{515}^{-1}-R_{770}^{-1}	Gitelson, Gritz, and Merzlyak (2003)
CRI3	R_{515}^{-1}-$R_{550}^{-1}\times R_{770}$	Gitelson, Gritz, and Merzlyak (2003)
CRI4	R_{515}^{-1}-$R_{700}^{-1}\times R_{770}$	Gitelson, Gritz, and Merzlyak (2003)
D1	D_{730}/D_{706}	Zarco-Tejada et al. (2003)
D2	D_{705}/D_{722}	Zarco-Tejada et al. (2003)
Datt	$(R_{850}$-$R_{710})/(R_{850}$-$R_{680})$	Datt (1999)
Datt2	R_{850}/R_{710}	Datt (1999)
Datt3	D_{754}/D_{704}	Datt (1999)
Datt4	$R_{672}/(R_{550}\times R_{708})$	Datt (1998)
Datt5	R_{672}/R_{550}	Datt (1998)
Datt6	$R_{860}/(R_{550}\times R_{708})$	Datt (1998)
DD	$(R_{749}$-$R_{720})$-$(R_{701}$-$R_{672})$	le Maire, François, and Dufrêne (2004)
DDn	$2\times(R_{710}$-R_{660}-$R_{760})$	le Maire et al. (2008)
DPI	$(D_{688}\times D_{710})/D_{697}^{2}$	Zarco-Tejada et al. (2003)
DWSI4	R_{550}/R_{680}	Apan et al. (2004)
GDVI 2	$(R_{800}^{2}$-$R_{680}^{2})/(R_{800}^{2}+ R_{680}^{2})$	Wu (2014)
GDVI 3	$(R_{800}^{3}$-$R_{680}^{3})/(R_{800}^{3}+ R_{680}^{3})$	Wu (2014)
GDVI 4	$(R_{800}^{4}$-$R_{680}^{4})/(R_{800}^{4}+ R_{680}^{4})$	Wu (2014)
GI	R_{554}/R_{677}	Smith et al. (1995)
Gitelson	R_{700}^{-1}	Gitelson, Buschmann, and Lichtenthaler (1999)
Gitelson2	$(R_{750}$-R_{800}/R_{695}-$R_{740})$-1	Gitelson, Gritz, and Merzlyak (2003)
GMI1	R_{750}/R_{550}	Gitelson, Gritz, and Merzlyak (2003)
GMI2	R_{750}/R_{700}	Gitelson, Gritz, and Merzlyak (2003)
Green NDVI	$(R_{800}$-$R_{550})/(R_{800}+ R_{550})$	Gitelson, Kaufman, and Merzlyak (1996)
Maccioni	$(R_{780}$-$R_{710})/(R_{780}$-$R_{680})$	Maccioni, Agati, and Mazzinghi (2001)
MCARI	$((R_{700}$-$R_{670})$-$0.2\times(R_{700}$-$R_{550}))\times(R_{700}/R_{670})$	Daughtry et al. (2000)
MCARI/OSAVI	*MCARI/OSAVI*	Daughtry et al. (2000)
MCARI2	$((R_{750}$-$R_{705})$-$0.2\times(R_{750}$-$R_{550}))\times(R_{750}/R_{705})$	Wu et al. (2008)
MCARI2/OSAVI2	*MCARI2/OSAVI2*	Wu et al. (2008)
MPRI	$(R_{515}$-$R_{530})/(R_{515}+ R_{530})$	Hernández-Clemente, Navarro-Cerrillo, and Zarco-Tejada (2012)
MSAVI	$0.5\times(2\times R_{800} + 1$-$((2\times R_{800} + 1)^2$–$8\times(R_{800}$-$R_{670}))^{0.5}$	Qi et al. (1994)
mSR2	(R_{750}/R_{705})-$1/(R_{750}/R_{705} + 1)^{0.5}$	Chen (1996)
MTCI	$(R_{754}$-$R_{709})/(R_{709}$-$R_{681})$	Dash and Curran (2004)
MTVI	$1.2\times(1.2\times(R_{800}$-$R_{550})$-$2.5\times(R_{670}$-$R_{550}))$	Haboudane et al. (2002)
NDVI	$(R_{800}$-$R_{680})/(R_{800}+ R_{680})$	Rouse et al. (1974)
NDVI2	$(R_{750}$-$R_{705})/(R_{750}+ R_{705})$	Gitelson and Merzlyak (1994)
NDVI3	$(R_{682}$-$R_{553})/(R_{682}+ R_{553})$	Gandia et al. (2004)
OSAVI	$(1 + 0.16)\times(R_{800}$-$R_{670})/(R_{800}+ R_{670} + 0.16)$	Rondeaux, Steven, and Baret (1996)
OSAVI2	$(1 + 0.16)\times(R_{750}$-$R_{705})/(R_{750}+ R_{705} + 0.16)$	Wu et al. (2008)
PARS	R_{746}/R_{513}	Chappelle, Kim, and McMurtrey (1992)
PRI	$(R_{531}$-$R_{570})/(R_{531}+ R_{570})$	Gamon, Peñuelas, and Field (1992)
PRI norm	$PRI/(RDVI\times R_{700}/R_{670})$	Zarco-Tejada et al. (2013)
PRI*CI2	$PRI\times CI2$	Garrity, Jan, and Vierling (2011)
PSSR	R_{800}/R_{635}	Blackburn (1998)
RDVI	$(R_{800}$-$R_{670})/\sqrt{(R_{800}+ R_{670})}$	Roujean and Breon (1995)
REP LE	Red-edge position through linear extrapolation	Cho and Skidmore (2006)
REP Li	$700 + 40\times(((R_{670}+ R_{780})/2$-$R_{700})/(R_{740}$-$R_{700}))$	Guyot and Baret (1988)
SAVI	$1.5\times(R_{800}$-$R_{670})/(R_{800}+ R_{670} + 0.5)$	Huete (1988)
SPVI	$0.4 \times 3.7\times(R_{800}$-$R_{670})$-$1.2\times((R_{530}$-$R_{670})^2)^{0.5}$	Vincini, Frazzi, and D'Alessio (2006)
SR	R_{800}/R_{680}	Jordan (1969)
SR1	R_{750}/R_{700}	Gitelson and Merzlyak (1997)
SR2	R_{752}/R_{690}	Gitelson and Merzlyak (1997)
SR3	R_{750}/R_{550}	Gitelson and Merzlyak (1997)
SR4	R_{700}/R_{670}	McMurtrey et al. (1994)
SR5	R_{675}/R_{700}	Chappelle, Kim, and McMurtrey (1992)
SR6	R_{750}/R_{710}	Zarco-Tejada and Miller (1999)
SR8	R_{515}/R_{550}	Hernández-Clemente et al. (2011)

(*Continued*)

Table 2. (Continued).

Index	Equation	Reference
Sum Dr1	$\sum_{R_{626}}^{R_{795}} \lvert D_{R_i} \rvert$	Elvidge and Chen (1995)
Sum Dr2	$\sum_{R_{680}}^{R_{780}} D_{R_i}$	Filella and Penuelas (1994)
TCARI	$3\times((R_{700}-R_{670})-0.2\times(R_{700}-R_{550})\times(R_{700}/R_{670}))$	Haboudane et al. (2002)
TCARI/OSAVI	$TCARI/OSAVI$	Haboudane et al. (2002)
TCARI2	$3\times((R_{750}-R_{705})-0.2\times(R_{750}-R_{550})\times(R_{750}/R_{705}))$	Wu (2014)
TCARI2/OSAVI2	$TCARI2/OSAVI2$	Wu (2014)
TVI	$0.5\times(120\times(R_{750}-R_{550})-200\times(R_{670}-R_{550}))$	Broge and Leblanc (2001)
Vogelmann	R_{740}/R_{720}	Vogelmann, Rock, and Moss (1993)
Vogelmann2	$(R_{734}-R_{747})/(R_{715}+R_{726})$	Vogelmann, Rock, and Moss (1993)
Vogelmann3	D_{715}/D_{705}	Vogelmann, Rock, and Moss (1993)
Vogelmann4	$(R_{734}-R_{747})/(R_{715}+R_{720})$	Vogelmann, Rock, and Moss (1993)

*$a = (R_{700}-R_{550})/150$; $b = R_{550}-(a*R_{550})$

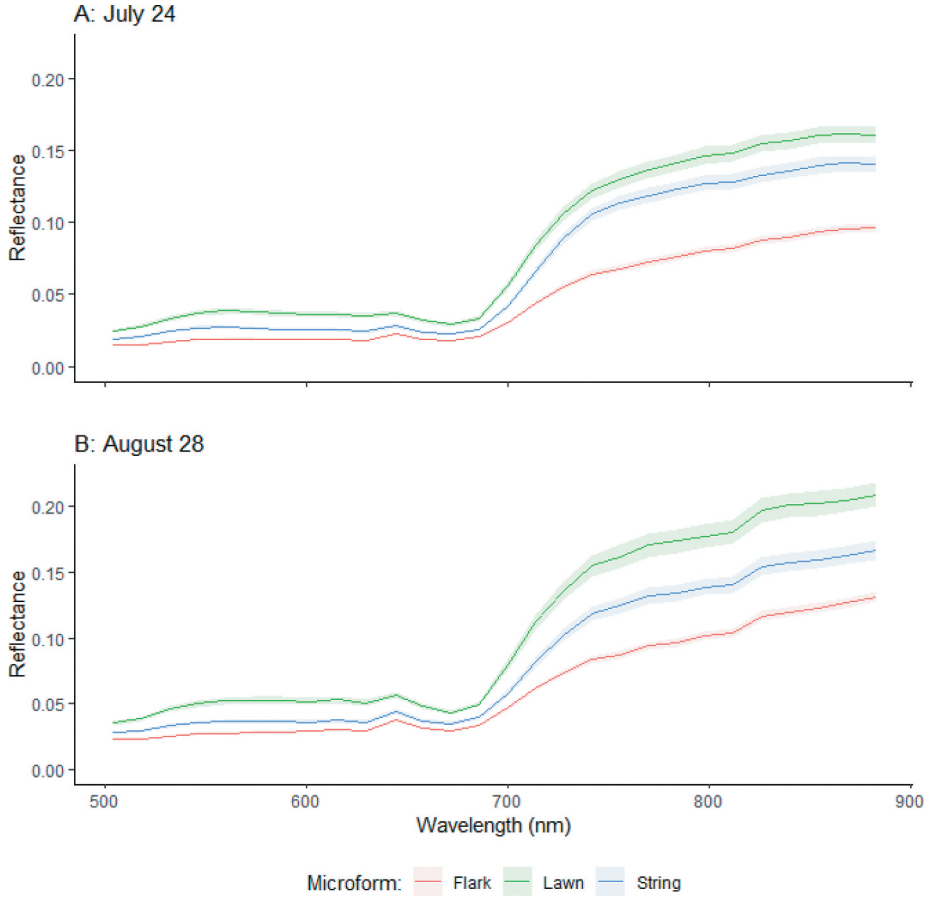

Figure 2. Reflectance curves for the vegetation plots inventoried in 2018, based on the hyperspectral drone images taken on A) July 24 and B) 28 August 2019. The vegetation plots were classified into three different microforms. Lines indicate mean values and shaded region mean ± standard error for the microforms.

forests (RF, Breiman 2001) regressions for the plots inventoried in 2018. RF has been used widely in biomass studies and it has often had the best goodness-of-fit (Poley and McDermid 2020); furthermore, it is insensitive to overfitting and can deal with a high number of cross-correlated features typical to hyperspectral data (Belgiu and Dragut 2016). We conducted regressions for each PFT and separately for the following summed up estimates: LAI for vascular plants in total, and biomass for vascular plants in total, mosses

in total and all plant species in total. To test the added value of hyperspectral drone data in mapping LAI and biomass, we tested regressions with three different feature sets for each plant species grouping: (1) all features, (2) hyperspectral features only, and (3) all other features than hyperspectral features.

To remove redundant and non-important features from the models, we reduced the number of features with an RF wrapper feature selection algorithm called Boruta (Kursa and Rudnicki 2010) before the final RF regressions. We used the mean decrease accuracy feature importance measure and chose those features that were not rejected during 999 RF runs (i.e. their importance was not significantly lower than those of randomly shuffled shadow features). We evaluated the relative importance of different features with the feature importance scores from Boruta.

We conducted 100 RF regressions for each plant species grouping and feature set option. In each regression, we used 500 trees and set the number of tested features at each node to one-third of features in the model. For each set of 100 regressions, we calculated minimum, maximum, and mean values of (1) the amount of variance explained (pseudo R^2 = 1 – (mean squared error)/variance(response)), (2) RMSE, and (3) nRMSE, with an out-of-bag evaluation in which approximately two-thirds of the data in each tree is used for training and the rest for evaluation (Breiman 2001). Earlier studies have shown that out-of-bag assessment gives an unbiased or even slightly conservative estimate of the model accuracy (Clark et al. 2010). Analyses were conducted in R (R Core Team 2018) using the packages randomForest (Liaw and Wiener 2002) and Boruta (Kursa and Rudnicki 2010).

We produced maps of LAI and biomass using a geographic object-based image analysis approach, since such an approach eases the integration of different datasets and delineates the landscape into meaningful vegetation patches (Blaschke et al. 2014). We segmented the 2016 drone image with the multiresolution segmentation algorithm by Baatz and Schäpe (2000) implemented in TerraView (Câmara et al. 2008). Before the segmentation, we generalized the drone image to 5 cm spatial resolution using bilinear interpolation. We gave equal weight to color and shape information as well as to compactness and smoothness and set the similarity threshold to 0.12 resulting in segments with an average size of 6 m^2 (minimum size 3.3 m^2). We then assigned LAI and biomass predictions of each RF model to each segment, estimated landscape-level LAI and biomass and compared the spatial pattern of LAI and biomass maps.

Results and discussion

Estimation of LAI and biomass from harvested samples

We could predict the PFT-specific LAI and biomass from samples harvested in 2014 with cover and height information with reasonably high accuracy (adjusted coefficient of determination between 0.50 and 0.98) Table 3. We applied these relationships to the plots inventoried in 2018 that were used as training data in remote sensing regressions. For the 2018 plots, mean LAI was 0.15 with the PFT-specific LAI estimate being the highest for graminoids Figure 3. Predicted biomass values were notably higher for mosses than for vascular plants, and the average value for total biomass was 260 g m^{-2} Figure 3.

There was a four-year lag between our field inventories; hence, yearly variation might provide some

Table 3. Equations for calculating leaf-area index and biomass based on harvested samples (n = 48), average and standard deviation values in the harvested data, and root mean squared error and adjusted coefficient of determination values.

	Leaf area index					Biomass				
Plant functional type	Equation	Mean ± sd (m^2 m^{-2})	RMSE (m^2 m^{-2})	nRMSE	R^2_{adj}	Equation	Mean ± sd (g m^{-2})	RMSE (g m^{-2})	nRMSE	R^2_{adj}
Evergreen shrub	LAI = 0.0138 + 0.0069*c	0.131 ± 0.148	0.052	0.09	0.87	BM = 3.51 + 1.35*c	26.4 ± 30.2	13.2	0.11	0.80
Deciduous shrub	LAI = −0.0012 + 0.0003*c*h	0.041 ± 0.127	0.018	0.02	0.98	BM = −0.63 + 0.12*c*h	17.1 ± 52.9	7.8	0.03	0.98
Forb	LAI = −0.0077 + 0.0010*c*h	0.078 ± 0.129	0.04	0.08	0.9	BM = −0.51 + 0.07*c*h	5.3 ± 8.9	3.2	0.07	0.86
Graminoid	LAI = 0.0420 + 0.0054*c	0.214 ± 0.099	0.064	0.15	0.56	BM = 15.40 + 0.45*c	30.0 ± 11.7	9.6	0.16	0.28
Sphagnum	n.a.	n.a.	n.a.	n.a.	n.a.	BM = −7.96 + 4.02*c	124.0 ± 182.8	83.0	0.11	0.79
Other moss	n.a.	n.a.	n.a.	n.a.	n.a.	BM = 4.36 + 1.89*c	88.7 ± 110.9	77.0	0.18	0.50
Total	n.a.	0.465 ± 0.325	n.a.	n.a.	n.a.	n.a.	291.5 ± 209.4	n.a.	n.a.	n.a.

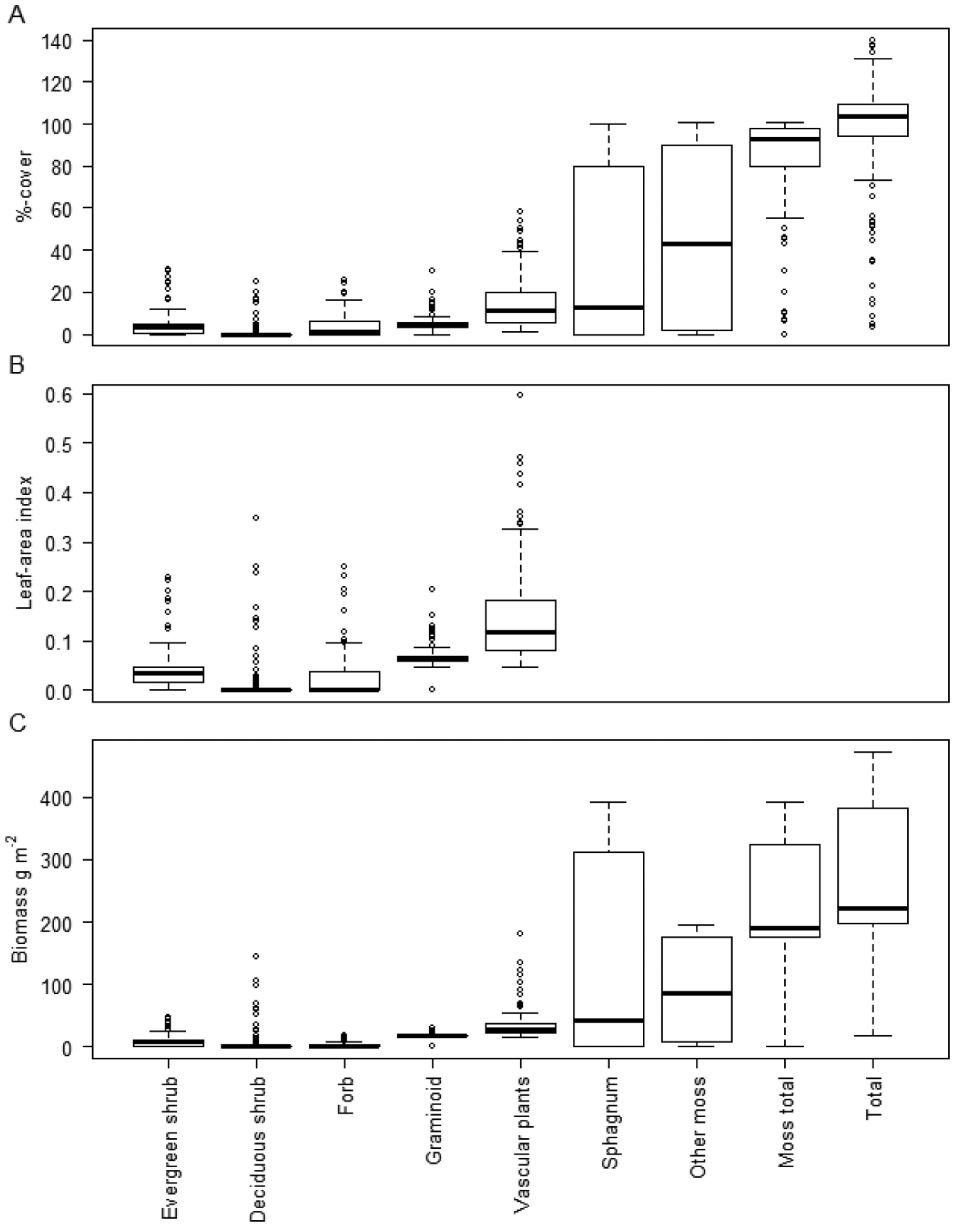

Figure 3. Box and whisker plots for A) measured percentage cover, B) estimated leaf-area index, and C) estimated biomass values for each plant functional type and total in vegetation plots inventoried in 2018 (n = 140).

uncertainties in our analysis. Nevertheless, during both field work years the relative abundance of different PFTs was similar (Table 3 and Figure 3) suggesting that yearly variation affects mostly the absolute biomass and LAI values and not their spatial patterns. Conversely, phenological stage may have a larger impact on the relative abundance of different PFTs (Juutinen et al. 2017; Cole, McMorrow, and Evans 2014) but in our case both field inventories were conducted during peak growing season. Furthermore, field work data from 2014 were used only to link PFT cover and height to biomass and LAI. Such relationships do not change rapidly in one study area and are also transferable and generalizable between study areas (Räsänen et al. 2019).

Remote sensing of total and PFT-specific LAI and biomass

In regressions between LAI and biomass and remote sensing data, the performance of the models varied markedly among different response variables (mean explained variance between −0.5% and 66.5%, Table 4). Remote sensing regressions functioned well for

total vascular LAI and biomass and relatively well for total biomass but there was more variation in PFT-specific regressions Tables 4 and 5.

Some PFTs could be predicted with relatively high accuracy (forbs, deciduous shrubs), and some with intermediate accuracy (evergreen shrubs). For graminoids, a low amount of variance was explained but RMSE was also low, while mosses had relatively high amount of explained variance and relatively high RMSE (Tables 4 and 5). On one hand, graminoids had low variance in LAI and biomass; i.e. there was a nearly contiguous graminoid cover in the landscape. On the other hand, mosses were abundant, could be observed from remote sensing data due to low vascular plant cover and had relatively high spatial variation of LAI and biomass Figure 3.

Many studies have concentrated on mapping cover and biomass of shrubs, which are abundant in many northern treeless environments (Greaves et al. 2016; Myers-Smith et al. 2015). In general, when a vegetation component is abundant and has relatively high variation in spatial patterns as well as distinct habitat and spectral and structural properties, it can be detected with remote sensing data more easily. There are notable differences between different northern treeless landscapes, including peatlands. In particular, when compared to our study area, some northern peatland landscapes have more (and some less) evident micro-topographical structure and higher (or lower) spatial variation vascular plant species abundance which is reflected in the ability to track the abundance and volume of different PFTs (Räsänen et al. 2020). Therefore, one limitation of our study was to concentrate only on one study area, and results could have been different in other sites.

The importance of hyperspectral and other remote sensing features

There was clear PFT-specific variation how much model performance improved when hyperspectral data were included in (Tables 4 and 5). The benefit of using hyperspectral data was the most evident for evergreen shrubs; models with hyperspectral features only had slightly better performance than models with all features (0.2–0.4%-point higher mean explained variance), whereas the performance was lower for the models omitting hyperspectral features (5.6–9.1%-point decrease in mean explained variance). Also for vascular LAI (5.3%-point increase in mean explained variance) and biomass (2.8%-point increase), total biomass (2.1%-point increase), forbs, graminoids, other mosses, and mosses in total the inclusion of hyperspectral data increased model performance, but the models with hyperspectral features only had 6.1–23.6%-point lower mean explained variance. For *Sphagnum*, the models omitting hyperspectral features and with all features had approximately equal performance, but models with hyperspectral features only had 5.1%-point lower mean explained variance. For deciduous shrubs, models with hyperspectral data had a very low performance (mean explained variance 0.0% and 0.1% for LAI and biomass, respectively), but models with all features had a moderate performance (mean explained variance

Table 4. Explained variance (%) in random forests regressions for leaf-area index and biomass for different plant functional types and total. For each plant species grouping and feature set options, minimum, maximum and mean (in parentheses) explained variance over 100 random forests regressions are given.

		Feature set		
Trait	Plant functional type	All features	Hyperspectral only	Hyperspectral omitted
Leaf–area index	Evergreen shrub	31.9–36.9 (34.3)	32.1–37.4 (34.7)	25.3–31.6 (28.7)
	Deciduous shrub	42.2–49.7 (46.1)	−3.1–3.0 (0.0)	56.7–64.1 (60.6)
	Forb	49.9–54.0 (51.8)	26.7–32.1 (29.3)	47.7–52.4 (49.9)
	Graminoid	12.4–18.1 (15.3)	1.0–8.3 (4.7)	9.0–17.1 (14.2)
	Vascular total	65.1–68.4 (66.5)	57.7–61.2 (59.2)	59.5–62.7 (61.2)
Biomass	Evergreen shrub	34.7–39.7 (36.9)	35.2–39.5 (37.1)	24.7–31.2 (27.8)
	Deciduous shrub	45.0–52.7 (49.3)	−5.7–4.2 (0.1)	54.1–63.1 (58.2)
	Forb	50.7–55.1 (53.1)	32.6–38.8 (35.3)	46.6–51.1 (48.8)
	Graminoid	−0.1–0.6 (0.3)	−0.3–0.4 (0.1)	−1.0–-0.2 (−0.5)
	Vascular total	60.8–65.9 (62.8)	35.9–42.2 (39.2)	57.5–62.3 (60.0)
	Sphagnum	60.4–62.9 (61.6)	55.3–58.2 (56.5)	59.7–62.9 (61.6)
	Other moss	55.3–58.1 (56.8)	46.1–48.8 (47.1)	54.5–57.5 (55.9)
	Moss total	47.3–51.4 (49.4)	40.2–43.4 (41.9)	44.8–48.5 (46.9)
	Total	47.2–51.1 (49.8)	41.3–45.6 (43.7)	47.3–50.7 (48.7)

Table 5. Root mean squared error (RMSE) and normalized RMSE (nRMSE) in random forests regressions for leaf-area index and biomass for different plant functional types and total. For each plant species grouping and feature set options, minimum, maximum and mean (in parentheses) RMSE and nRMSE over 100 random forests regressions are given.

		Feature set					
		All features		Hyperspectral only		Excluding hyperspectral	
Trait	Plant functional type	RMSE	nRMSE	RMSE	nRMSE	RMSE	nRMSE
Leaf–area index	Evergreen shrub	0.035–0.037 (0.036)	0.15–0.16 (0.16)	0.035–0.036 (0.036)	0.15–0.16 (0.16)	0.037–0.038 (0.037)	0.16–0.17 (0.16)
	Deciduous shrub	0.034–0.035 (0.035)	0.10–0.10 (0.10)	0.047–0.049 (0.048)	0.13–0.14 (0.14)	0.029–0.031 (0.030)	0.08–0.09 (0.09)
	Forb	0.031–0.033 (0.032)	0.12–0.13 (0.13)	0.038–0.040 (0.039)	0.15–0.16 (0.16)	0.032–0.033 (0.033)	0.13–0.13 (0.13)
	Graminoid	0.022–0.023 (0.023)	0.11–0.11 (0.11)	0.023–0.024 (0.024)	0.11–0.12 (0.12)	0.022–0.023 (0.023)	0.11–0.11 (0.11)
	Vascular total	0.055–0.058 (0.056)	0.10–0.11 (0.10)	0.061–0.063 (0.062)	0.11–0.11 (0.11)	0.060–0.062 (0.061)	0.11–0.11 (0.11)
Biomass	Evergreen shrub	6.9–7.2 (7.1)	0.15–0.16 (0.16)	6.9–7.2 (7.1)	0.15–0.16 (0.16)	7.4–7.7 (7.6)	0.16–0.17 (0.17)
	Deciduous shrub	13.7–14.7 (14.1)	0.09–0.10 (0.10)	19.4–20.4 (20.0)	0.13–0.14 (0.14)	12.1–13.4 (12.8)	0.08–0.09 (0.09)
	Forb	2.1–2.2 (2.1)	0.13–0.13 (0.13)	2.4–2.6 (2.5)	0.14–0.15 (0.15)	2.2–2.3 (2.2)	0.13–0.14 (0.13)
	Graminoid	2.4–2.5 (2.5)	0.08–0.09 (0.09)	2.5–2.5 (2.5)	0.09–0.09 (0.09)	2.5–2.6 (2.6)	0.09–0.09 (0.09)
	Vascular total	13.8–14.8 (14.4)	0.08–0.09 (0.09)	17.9–18.9 (18.4)	0.11–0.12 (0.11)	14.5–15.4 (14.9)	0.09–0.09 (0.09)
	Sphagnum	95.7–98.9 (97.3)	0.24–0.25 (0.25)	101.6–105.0 (103.6)	0.26–0.27 (0.26)	95.7–99.8 (97.3)	0.24–0.25 (0.25)
	Other moss	49.9–51.5 (50.6)	0.25–0.26 (0.26)	55.1–56.6 (56.0)	0.28–0.29 (0.29)	50.2–52.0 (51.1)	0.26–0.27 (0.26)
	Moss total	75.5–78.6 (77.0)	0.19–0.20 (0.20)	81.5–83.7 (82.5)	0.21–0.21 (0.21)	77.7–80.4 (78.9)	0.20–0.20 (0.20)
	Total	78.8–81.9 (79.9)	0.17–0.18 (0.18)	83.1–86.3 (84.6)	0.18–0.19 (0.19)	79.2–81.7 (80.7)	0.17–0.18 (0.18)

46.1% and 49.3% for LAI and biomass, respectively), and models omitting hyperspectral features even better performance (58.2% and 60.6% for LAI and biomass, respectively) Table 4.

In the models with all features, peak growing season vegetation indices calculated from hyperspectral data, drone topography, wetter year drone green and red band, GLCM Haralick correlation and drone vegetation height were among the most important ones Figure 4a. In the models with hyperspectral features only, peak growing season features were typically more important than late summer features but also late summer features were deemed important in many regressions Figure 4b. When we omitted hyperspectral data from the regressions, drone spectral, textural, topographic, and vegetation height features were among the most important but also aerial imagery features, in particular the near-infrared band, and early and midsummer PlanetScope features were among the most important ones Figure 4c. Hyperspectral coefficient of variation, lidar, and late summer PlanetScope features had low importance and were often rejected by Boruta.

Our hyperspectral data included only 28 spectral bands in a relatively narrow spectral range (500–-900 nm). If the data would have included more bands with narrower bandwidth and wider spectral range in total, the results could have been different and the importance of hyperspectral data more evident. Nonetheless, in a previous study by Harris, Charnock, and Lucas (2015) which utilized airborne hyperspectral data for mapping peatland vegetation gradients, it was found that relatively few bands (12 or 16) were selected for final regression models. In another study, Turner et al. (2019) assessed optimal spatial and spectral resolution for mapping health of Antarctic moss vegetation with different drone-based multispectral and hyperspectral sensors and concluded that 25 VNIR bands at 8 cm spatial resolution was an ideal band constellation. These findings suggest that hundreds of bands are not necessarily needed when mapping vegetation patterns in peatlands and similar landscapes. However, if the goal is to identify individual plant species instead of PFTs, better spectral resolution might aid more as some

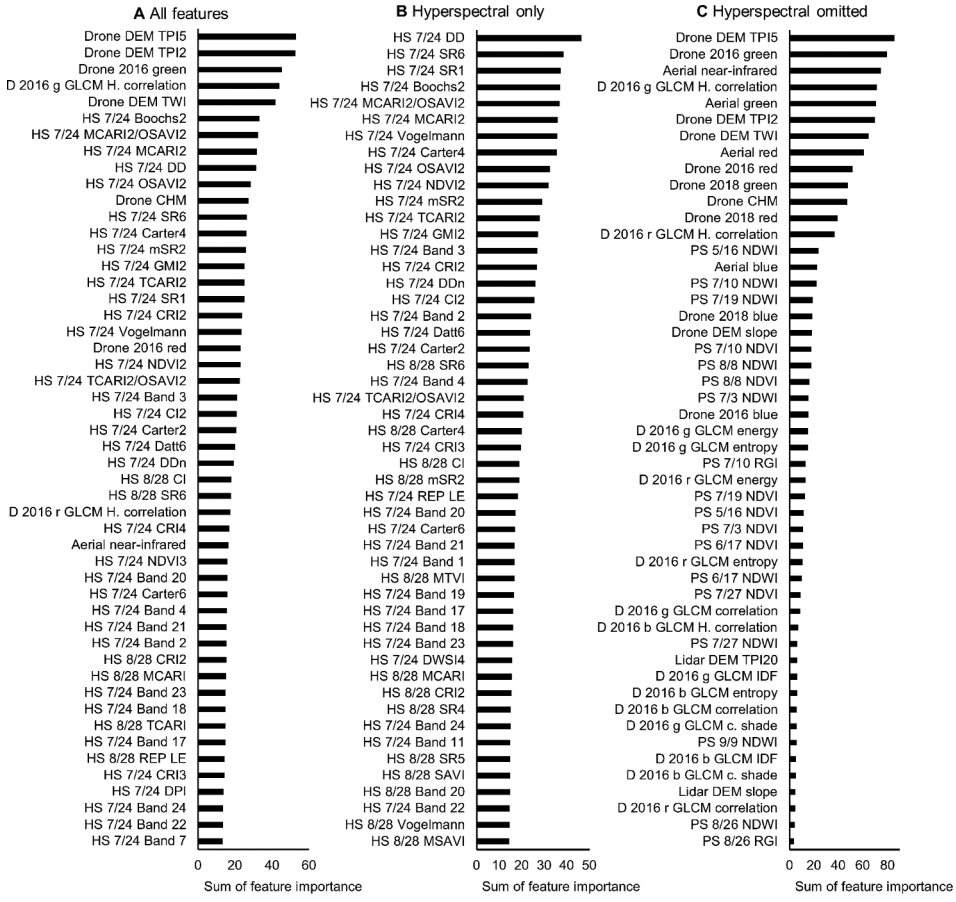

Figure 4. Sum of Boruta feature importance scores for the 50 most important features over all regressions with A) all features, B) hyperspectral features only, and C) hyperspectral features omitted. In the figure, HS refers to hyperspectral, other abbreviations are listed in Tables 1, 2 and S1.

species have their own specific spectral signatures (Falcioni et al. 2020).

Our results suggest that some of the differences in vegetation cannot be delineated with spectral data; instead, also structural and topographic features are needed to obtain the highest accuracies Tables 4 and 5. Similar results have been obtained also previously in studies utilizing hyperspectral data (Arroyo-Mora et al. 2017; Luo et al. 2016; Sankey et al. 2018; Yue et al. 2017; Li et al. 2020). This is evident in particular with deciduous shrubs, which could not be mapped with hyperspectral data only; i.e. the models had very low explanatory capacities Table 4 and predicted values relatively high variance Table 6. Instead, for this PFT, the most important remote sensing features included topographic and vegetation height features derived from SfM drone data. This suggests that deciduous shrub abundance follows micro-topographic variation within the fen landscape, with the deciduous shrubs being most abundant in strings. Therefore, our results highlight that both topographic and spectral features should be used when mapping vegetation in patterned fen landscapes. Nevertheless, not all vegetation follows the micro-topography and there is also a notable variation of vegetation (and thus spectral signatures) within the different micro-forms; part of which can be tracked with high-resolution spectral data. This is evident in particular with evergreen shrubs, for which the highest explanatory capacities were obtained with hyperspectral features only Table 4.

According to our results, a majority of the most important features were calculated from ultra-high resolution datasets (spatial resolution <10 cm), and the less fine-resolution data with a spatial resolution of 0.5–3.0 m were not as important Figure 4. Similar patterns could be observed both for spectral and structural/topographic features: data from aerial and satellite platforms were of less importance than drone data. Therefore, our results support previous findings

Table 6. Landscape-level mean (± standard deviation) leaf-area index and biomass for plant functional type-specific and total estimates based on maps produced with different feature sets.

		Feature set		
Trait	Plant functional type	All features	Hyperspectral only	Hyperspectral omitted
Leaf-area index	Deciduous shrub	0.012 ± 0.013	0.014 ± 0.025	0.012 ± 0.013
	Evergreen shrub	0.038 ± 0.018	0.048 ± 0.024	0.036 ± 0.02
	Forb	0.034 ± 0.031	0.033 ± 0.024	0.026 ± 0.032
	Graminoid	0.069 ± 0.007	0.070 ± 0.012	0.070 ± 0.008
	Vascular total	0.166 ± 0.062	0.187 ± 0.071	0.149 ± 0.053
Biomass (g m^{-2})	Deciduous shrub	5.3 ± 5.9	5.7 ± 9.5	4.7 ± 5.8
	Evergreen shrub	8.2 ± 4.1	8.1 ± 4.1	8.1 ± 4.2
	Forb	2.4 ± 2.2	2.4 ± 1.8	1.8 ± 2.2
	Graminoid	17.7 ± 0.6	17.7 ± 0.7	17.1 ± 0.6
	Vascular total	35.1 ± 11.6	39.5 ± 16.4	33.1 ± 10
	Sphagnum	104.5 ± 109.4	100.2 ± 104.4	112.9 ± 112.1
	Other moss	99.2 ± 55.3	100.9 ± 53.4	97.1 ± 52.8
	Moss total	198.9 ± 74.8	200.4 ± 69.6	211.8 ± 64.7
	Total	236.3 ± 78.6	235.5 ± 76.9	247.9 ± 71.3

that drone-derived DTMs can reveal fine-scale variation in micro-topography which controls vegetation patterns and ecosystem functioning in flat peatland landscapes (Harris and Baird 2019; Moore et al. 2019), and drone imagery can be used to track peatland vegetation (Palace et al. 2018; Beyer et al. 2019). Yet, the importance of ultra-high-resolution data is contradicted by our earlier results indicating that as high land cover mapping accuracies can be achieved with 50 cm spatial resolution data than with <10 cm spatial resolution data in a relatively similar type of peatland landscape (Räsänen and Virtanen 2019). However, in that study, only RGB drone imagery instead of hyperspectral data were used and land cover instead of biomass and leaf-area index was mapped. Although our study highlighted the importance of ultra-high-resolution datasets, also coarser-resolution features were among the most important in some regressions Figure 4, in particular in regressions omitting hyperspectral data. In these regressions, aerial imagery and PlanetScope provided spectral information with an infrared band that could not be obtained with RGB drone data.

We utilized only one ultra-high resolution vegetation structural feature (mean vegetation height based on SfM photogrammetry), which was important in particular for deciduous shrub LAI and biomass prediction. However, its value was more limited for other regressions. In the visual interpretation of the vegetation height model, it could be seen that the height of forbs and graminoids was not accurately predicted, and higher values for vegetation height were located in strings with higher shrub cover; moreover, the location of trees in strings was quite well predicted. In earlier studies, SfM-based vegetation height models have been used, for example, in predicting biomass patterns in temperate arid environments with some trees, tall shrubs and grass tussocks (Cunliffe, Brazier, and Anderson 2016), biomass patterns in shrub-dominated tundra (Cunliffe et al. 2020), and in estimating vegetation height of shrubs in low-arctic tundra (Fraser, Ian Olthof, and Schmitt 2016). In all of these studies, the spatial resolution has been ≤1 cm compared to 9 cm in our study. A finer spatial resolution could thus help in achieving a more accurate prediction of height and volume of different PFTs, and from a finer resolution data, more features than only mean height could have been quantified. Even better results could be achieved with terrestrial or ultra-high resolution aerial/drone-based lidar (Greaves et al. 2016, 2017; Sankey et al. 2018), which has outperformed SfM in prediction accuracy in forested areas due to the capability to map terrain elevation below dense canopies (Wallace et al. 2016). Therefore, future research avenues could include mapping of ultra-high resolution of vegetation structure for different PFTs, and comparison of different methods such as SfM and lidar in open treeless environments. However, in peatlands where a majority of total biomass is composed of mosses, structural features should be coupled with spectral features.

Only a part of the remote sensing data was from the same year when the field inventory training data for remote sensing was collected (i.e. 2018, Table 1), which could potentially lead to errors in LAI and biomass prediction. Despite this fact, RGB drone features from the field work year of 2018 had lower importance in the regressions than RGB drone features

from the wetter year of 2016 Figure 4, when vegetation was more abundant and there was higher contrast in the image. As both images were taken during the peak growing season, it can be reasoned that remote sensing data may not need to be from the same year if it is taken during similar phenological stage. In previous research in peatland landscapes, it has been shown that during peak growing season, vegetation volume is at its highest and plant functional types are spectrally separable from each other (Cole, McMorrow, and Evans 2014) and that spatial patterns of biomass and LAI vary throughout the phenological cycle (Juutinen et al. 2017). According to our feature importance results in Figure 4, peak growing season hyperspectral and PlanetScope features were more important than non-peak season features. However, also non-peak season features and RGB drone features from two different years (2016 and 2018) were important in the different regressions Figure 4. This indicates that multitemporal data can alleviate problems related to temporal mismatches and increase model performance (Räsänen et al. 2020; Halabisky, Babcock, and Moskal 2018; Gholizadeh et al. 2020; Poley and McDermid 2020). Nevertheless, there is some uncertainty when comparing the relative benefit of datasets with divergent spectral and spatial resolutions as the data were acquired at different times; in an ideal situation, all datasets would have been collected simultaneously. Multi-temporal datasets could also be integrated with temporal models utilizing environmental parameters such as maximum ecosystem photosynthesis or climatic data but the use of such models would require also multitemporal vegetation inventories (Juutinen et al. 2017).

When looking at the reflectance spectra of the hyperspectral images Figure 2, reflectance at all wavelengths was higher in the late growing season than during peak season which might indicate that conversion to absolute reflectance values was imperfect with the reflectance plates, which might affect results of the benefit of hyperspectral data. However, the reflectance differences between the images were higher in the visible spectrum, and therefore, consistent with earlier literature, spectral indices such as NDVI, MERIS terrestrial chlorophyll index (MTCI, Dash and Curran 2004) and red-edge position (Cho and Skidmore 2006) dropped between peak season and late season showing the start of senescence (Cole, McMorrow, and Evans 2014; Harris and Dash 2011). The drop was more evident in strings that have higher vascular plant cover than moss-dominated lawns and flarks indicating that leaf senescence of deciduous vegetation and decrease in chlorophyll affected vascular plants more than mosses. This finding is backed by previous research in which it has been found that phenology derived changes in reflectance are higher in shrubs and other vascular plants than in mosses (Cole, McMorrow, and Evans 2014).

Landscape-level estimates of LAI and biomass

Overall, LAI and biomass estimates with remote sensing regressions with three different feature sets were typically quite close to each other, yet there was some variation between patches and landscape in total Table 6, Figures 5 and 6. The differences in estimates were relatively small between the three different feature set options (all data, hyperspectral only, hyperspectral omitted) when we predicted total or moss biomass Table 6, Figure 5(d–f), Figures 6(f–h). There was only some overestimation in regressions omitting hyperspectral data. In *Sphagnum* biomass regressions, hyperspectral regressions had slight underestimation and regressions without hyperspectral features overestimation Table 6. As also the explanatory capacities were relatively high in moss and total biomass regressions, it can be suggested that all three feature set options can be used for operational purposes. For vascular plants, the differences in plot and landscape-level estimates were higher Table 6, Figures 5(a–c), Figures 6(a–c). When compared to models with all features, regressions with hyperspectral data only overestimated in particular deciduous shrub and total LAI and biomass as well as evergreen shrub LAI, whereas regressions omitting hyperspectral data underestimated forb and total LAI and biomass as well as deciduous shrub biomass Table 6.

Vascular LAI patterns followed the micro-topographical variation in the fen landscape with the highest values being in the strings Figures 6(a–c, e), whereas for total biomass, the highest values were found in those lawn and string patches that had continuous moss cover Figures 6(f–h). When our ultra-high resolution biomass maps were compared with biomass maps produced with 2 m spatial resolution satellite imagery in the same site (Räsänen et al. 2019), the string-flark pattern was better distinguished on the finer-resolution maps, further suggesting the benefits of using ultra-high spatial resolution data.

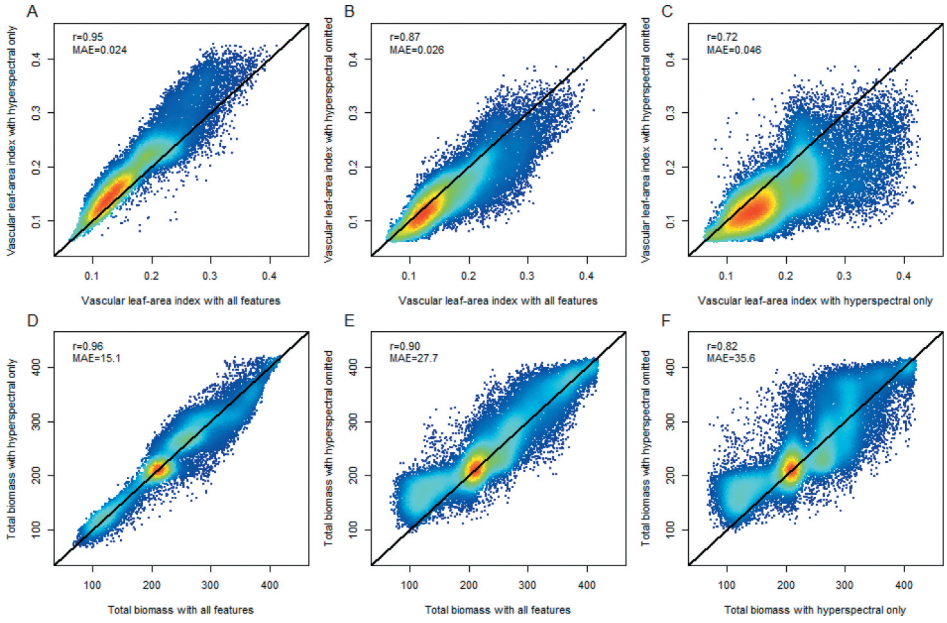

Figure 5. Pairwise map comparisons for vascular leaf-area index (A–C) and total biomass (D–F) for regressions with different feature sets. Each dot in the plots represents LAI or biomass prediction for one segment. Dot density is showed with heat map colors so that red indicates higher density and blue lower density. In the figure, r refers to Pearson correlation coefficient and MAE to mean absolute error between the maps.

Our overall estimates of vascular LAI and biomass Figures 3, 5 and 6 were lower compared to previous coarser resolution estimates in the study area (Räsänen et al. 2019) and other estimates in similar peatland landscapes (Wilson et al. 2007; Laine et al. 2019). This is related to the dry and warm year in 2018 (Fig. S1) during which the cover and volume of vascular plants were low and the training data for remote sensing analyses were collected. However, as already discussed in Section "Estimation of LAI and biomass from harvested samples" the yearly variation affected the total abundance and volume of different PFTs but not their relative abundance nor spatial patterns. Thus, we judge that the absolute LAI and biomass values could have been better predicted remote sensing data concurrent with field work but the spatial patterns can be well predicted with asynchronous data.

Our analysis excluded trees as we did not have suitable training data for predicting tree LAI and biomass. Few trees found in the study area are growing only in strings and are a minor component of vegetation; moreover, as there were no trees in our field plots, they had no impact on our model parameters. If the goal would be the prediction of tree LAI and biomass, it should be pursued separately from other PFTs in particular in these kinds of landscapes with few trees, and in the prediction, ultra-high-resolution vegetation height model should be utilized (Cunliffe, Brazier, and Anderson 2016; Cunliffe et al. 2020; Wallace et al. 2016).

Conclusions

We evaluated how well-peatland LAI and biomass patterns can be detected with multi-source and multi-temporal ultra-high-resolution remote sensing data and examined the benefit of hyperspectral drone data. The remote sensing-based regression models for total vascular LAI and biomass had a relatively high explanatory capacity, and also the model for total biomass functioned moderately well, suggesting good detectability of LAI and biomass patterns with ultra-high resolution remote sensing in spatially heterogeneous landscapes such as northern peatlands. There was more variation in PFT-specific models. As explanatory capacities were higher for total LAI and biomass than for PFT-specific estimates, our results suggest that maps of total LAI and biomass should not be summed maps of PFT-specific estimates but the response variable in the regressions and maps should be the total LAI or biomass. These maps could then be complemented with maps for such

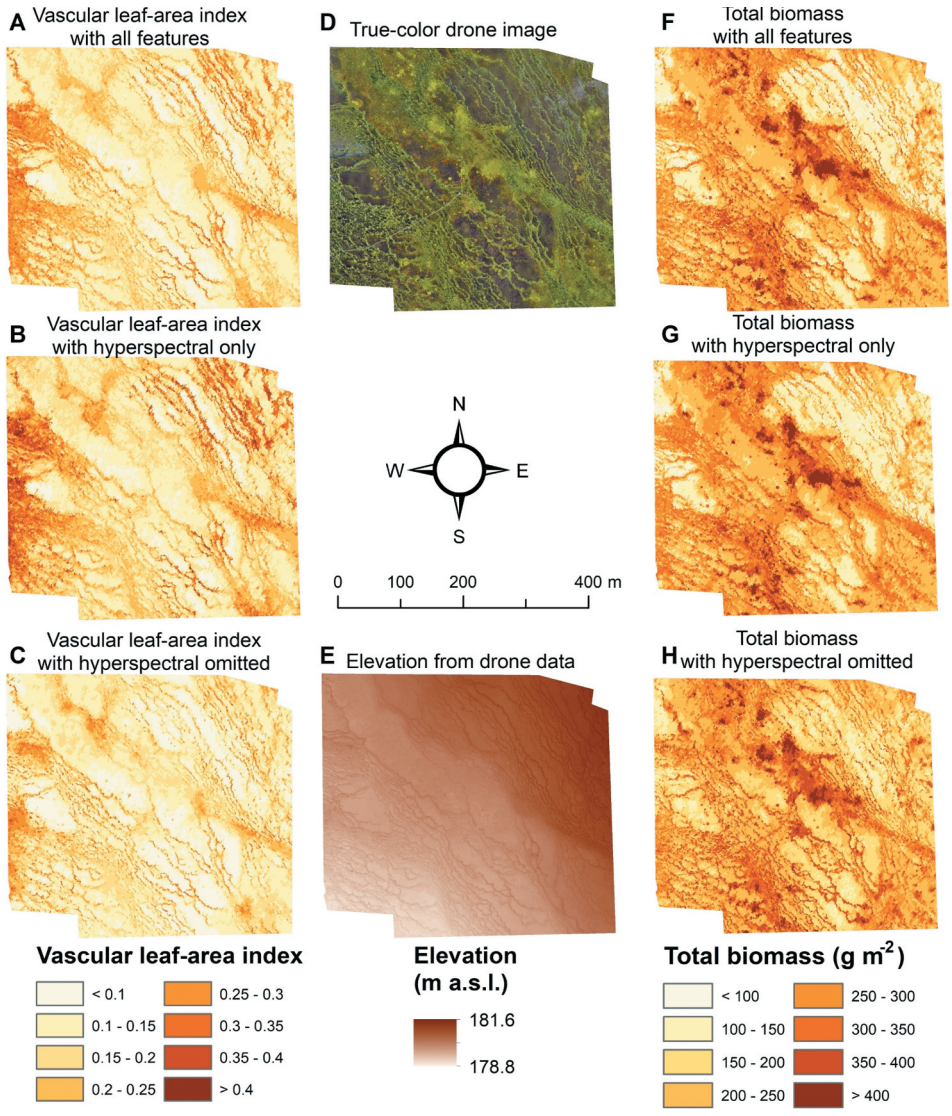

Figure 6. Maps of vascular leaf-area index (A–C) and total biomass (F–H) with different feature sets used as the input data. Additionally, a true-color drone image from 2016 (D) and elevation based on drone data (E) are included.

PFTs that can be mapped with relatively high accuracy.

Our results showed mixed results on whether hyperspectral drone data are important in tracking LAI and biomass patterns. According to feature importance scores, hyperspectral data were extremely important; yet, when looking at explanatory capacities of different models, the inclusion of hyperspectral data boosted performance in most models but usually rather modestly. Additionally, landscape-level LAI and biomass estimates regressions with three different feature sets (all features, hyperspectral features, hyperspectral omitted) were typically quite close to each other. These results suggest that hyperspectral data give only slight benefits when included in a multi-source remote sensing analysis of LAI and aboveground biomass patterns. In future studies, the relative benefit of different multispectral and hyperspectral sensors with various band constellations and spectral ranges could be tested in different landscapes.

Our results showed that multiple different remote sensing datasets are important in LAI and biomass estimation; hence, we suggest that (hyper)spectral datasets should be combined with topographic and structural data at sub-meter-level spatial resolution when mapping vegetation patterns in spatially heterogeneous landscapes such as northern peatlands. We also found that peak growing season features were more important than non-peak season features

but more research should be conducted for evaluating the optimal timing for remote sensing data acquisition.

Acknowledgements

We thank Hanna Hyvönen and Olivia Kuuri-Riutta for assisting in field data collection. The work was supported by the Academy of Finland (grants 296,423 [AR, SJ, TV], 308,513 [AR, TV], 296,888 and 314,799 [MA]) and Helsinki Institute of Sustainability Science visitor grant [SJ, MK].

Funding

This work was supported by the Suomen Akatemia [296423, 308513, 296888, 314799]; Helsingin Yliopisto.

ORCID

Aleksi Räsänen http://orcid.org/0000-0002-3629-1837
Sari Juutinen http://orcid.org/0000-0002-7752-1950
Margaret Kalacska http://orcid.org/0000-0002-1676-481X
Mika Aurela http://orcid.org/0000-0002-4046-7225

Data availability

The data that support the findings of this study are available from the corresponding author, AR, upon reasonable request.

References

Aasen, H., and A. Bolten. 2018. "Multi-temporal High-resolution Imaging Spectroscopy with Hyperspectral 2D Imagers – From Theory to Application." *Remote Sensing of Environment* 205: 374–389. doi:10.1016/j.rse.2017.10.043.

Aasen, H., A. Burkart, A. Bolten, and G. Bareth. 2015. "Generating 3D Hyperspectral Information with Lightweight UAV Snapshot Cameras for Vegetation Monitoring: From Camera Calibration to Quality Assurance." *ISPRS Journal of Photogrammetry and Remote Sensing* 108: 245–259. doi:10.1016/j.isprsjprs.2015.08.002.

Apan, A., A. Held, S. Phinn, and J. Markley. 2004. "Detecting Sugarcane 'Orange Rust' Disease Using EO-1 Hyperion Hyperspectral Imagery." *International Journal of Remote Sensing* 25 (2): 489–498. doi:10.1080/01431160310001618031.

Arroyo-Mora, J. P., M. Kalacska, O. Lucanus, R. Soffer, and G. Leblanc. 2017. "Spectro-spatial Relationship between UAV Derived High Resolution DEM and SWIR Hyperspectral Data: Application to an Ombrotrophic Peatland." Paper presented at the Proceedings of SPIE - The International Society for Optical Engineering, Remote Sensing for Agriculture, Ecosystems, and Hydrology XIX, Warsaw, Poland, 104210P.

Arroyo-Mora, J. P., M. Kalacska, D. Inamdar, R. Soffer, O. Lucanus, J. Gorman, T. Naprstek, et al.. 2019. "Implementation of a UAV–Hyperspectral Pushbroom Imager for Ecological Monitoring." *Drones* 3 (1): 12. DOI:10.3390/drones3010012.

Baatz, M., and A. Schäpe. 2000. "Multiresolution Segmentation – An Optimization Approach for High Quality Multi-scale Image Segmentation." In *Angewandte Geographische Informations-Verarbeitung XII*, edited by J. Strobl, T. Blaschke, and G. Griesebner, 12–23. Karlsruhe, Germany: Wichmann Verlag.

Basnyat, P., B. McConkey, G. P. Lafond, A. Moulin, and Y. Pelcat. 2004. "Optimal Time for Remote Sensing to Relate to Crop Grain Yield on the Canadian Prairies." *Canadian Journal of Plant Science* 84 (1): 97–103. doi:10.4141/p03-070.

Belgiu, M., and L. Dragut. 2016. "Random Forest in Remote Sensing: A Review of Applications and Future Directions." *ISPRS Journal of Photogrammetry and Remote Sensing* 114: 24–31. doi:10.1016/j.isprsjprs.2016.01.011.

Berner, L. T., P. Jantz, K. D. Tape, and S. J. Goetz. 2018. "Tundra Plant Aboveground Biomass and Shrub Dominance Mapped across the North Slope of Alaska." *Environmental Research Letters* 13 (3): 035002. doi:10.1088/1748-9326/aaaa9a.

Beyer, F., G. Jurasinski, J. Couwenberg, and G. Görres. 2019. "Multisensor Data to Derive Peatland Vegetation Communities Using a Fixed-wing Unmanned Aerial Vehicle." *International Journal of Remote Sensing* 40 (24): 9103–9125. doi:10.1080/01431161.2019.1580825.

Blackburn, G. A. 1998. "Quantifying Chlorophylls and Caroteniods at Leaf and Canopy Scales: An Evaluation of Some Hyperspectral Approaches." *Remote Sensing of Environment* 66 (3): 273–285. doi:10.1016/S0034-4257(98)00059-5.

Blaschke, T., G. J. Hay, M. Kelly, S. Lang, P. Hofmann, E. Addink, R. Q. Feitosa, F. van der Meer, H. van der Werff, and F. van Coillie. 2014. "Geographic Object-based Image Analysis–towards a New Paradigm." *ISPRS Journal of Photogrammetry and Remote Sensing* 87: 180–191. doi:10.1016/j.isprsjprs.2013.09.014.

Böhner, J., and T. Selige. 2006. "Spatial Prediction of Soil Attributes Using Terrain Analysis and Climate Regionalisation." In *SAGA – Analysis and Modelling Applications. Göttinger Geographische Abhandlungen 115.*, edited by J. Böhner, K. R. McCloy, and J. Strobl, 13–28. Göttingen, Germany: Geographisches Institut der Universität Göttingen.

Boochs, F., G. Kupfer, K. Dockter, and W. Kühbauch. 1990. "Shape of the Red Edge as Vitality Indicator for Plants." *International Journal of Remote Sensing* 11 (10): 1741–1753. doi:10.1080/01431169008955127.

Breiman, L. 2001. "Random Forests." *Machine Learning* 45 (1): 5–32. doi:10.1023/a:1010933404324.

Broge, N. H., and E. Leblanc. 2001. "Comparing Prediction Power and Stability of Broadband and Hyperspectral Vegetation Indices for Estimation of Green Leaf Area Index and Canopy Chlorophyll Density." *Remote Sensing of Environment* 76 (2): 156–172. doi:10.1016/S0034-4257(00)00197-8.

Câmara, G., L. Vinhas, K. R. Ferreira, G. R. De Queiroz, R. C. M. De Souza, A. M. V. Monteiro, M. T. De Carvalho, M. A. Casanova, and U. M. De Freitas. 2008. "TerraLib: An Open Source GIS Library for Large-Scale Environmental and Socio-Economic Applications." In *Open Source Approaches in Spatial Data Handling*, edited by G. Brent Hall and M. G. Leahy, 247–270. Berlin, Heidelberg: Springer Berlin Heidelberg.

Carter, G. A. 1994. "Ratios of Leaf Reflectances in Narrow Wavebands as Indicators of Plant Stress." *International Journal of Remote Sensing* 15 (3): 697–703. doi:10.1080/01431169408954109.

Chapin, F. S., III, M. S. Bret-Harte, S. E. Hobbie, and H. Zhong. 1996. "Plant Functional Types as Predictors of Transient Responses of Arctic Vegetation to Global Change." *Journal of Vegetation Science* 7 (3): 347–358. doi:10.2307/3236278.

Chappelle, E. W., M. S. Kim, and J. E. McMurtrey. 1992. "Ratio Analysis of Reflectance Spectra (RARS): An Algorithm for the Remote Estimation of the Concentrations of Chlorophyll A, Chlorophyll B, and Carotenoids in Soybean Leaves." *Remote Sensing of Environment* 39 (3): 239–247. doi:10.1016/0034-4257(92)90089-3.

Chen, B., L. Chen, M. Lu, and B. Xu. 2017. "Wetland Mapping by Fusing Fine Spatial and Hyperspectral Resolution Images." *Ecological Modelling* 353: 95–106. doi:10.1016/j.ecolmodel.2017.01.004.

Chen, B., B. Huang, and B. Xu. 2017. "Multi-source Remotely Sensed Data Fusion for Improving Land Cover Classification." *ISPRS Journal of Photogrammetry and Remote Sensing* 124: 27–39. doi:10.1016/j.isprsjprs.2016.12.008.

Chen, J. M. 1996. "Evaluation of Vegetation Indices and a Modified Simple Ratio for Boreal Applications." *Canadian Journal of Remote Sensing* 22 (3): 229–242. doi:10.1080/07038992.1996.10855178.

Cho, M. A., and A. K. Skidmore. 2006. "A New Technique for Extracting the Red Edge Position from Hyperspectral Data: The Linear Extrapolation Method." *Remote Sensing of Environment* 101 (2): 181–193. doi:10.1016/j.rse.2005.12.011.

Clark, M. L., T. Mitchell Aide, H. Ricardo Grau, and G. Riner. 2010. "A Scalable Approach to Mapping Annual Land Cover at 250 M Using MODIS Time Series Data: A Case Study in the Dry Chaco Ecoregion of South America." *Remote Sensing of Environment* 114 (11): 2816–2832. doi:10.1016/j.rse.2010.07.001.

Cole, B., J. McMorrow, and M. Evans. 2013. "Empirical Modelling of Vegetation Abundance from Airborne Hyperspectral Data for Upland Peatland Restoration Monitoring." *Remote Sensing* 6 (1): 716–739. doi:10.3390/rs6010716.

Cole, B., J. McMorrow, and M. Evans. 2014. "Spectral Monitoring of Moorland Plant Phenology to Identify a Temporal Window for Hyperspectral Remote Sensing of Peatland." *ISPRS Journal of Photogrammetry and Remote Sensing* 90: 49–58. doi:10.1016/j.isprsjprs.2014.01.010.

Conrad, O., B. Bechtel, M. Bock, H. Dietrich, E. Fischer, L. Gerlitz, J. Wehberg, V. Wichmann, and J. Böhner. 2015. "System for Automated Geoscientific Analyses (SAGA) V. 2.1.4." *Geoscientific Model Development* 8 (7): 1991–2007. doi:10.5194/gmd-8-1991-2015.

Coops, N. C., M. Johnson, M. A. Wulder, and J. C. White. 2006. "Assessment of QuickBird High Spatial Resolution Imagery to Detect Red Attack Damage Due to Mountain Pine Beetle Infestation." *Remote Sensing of Environment* 103 (1): 67–80. doi:10.1016/j.rse.2006.03.012.

Cunliffe, A. M., J. J. Assmann, G. Daskalova, J. T. Kerby, and I. H. Myers-Smith. 2020. "Aboveground Biomass Corresponds Strongly with Drone-derived Canopy Height but Weakly with Greenness (NDVI) in a Shrub Tundra Landscape." *Environmental Research Letters*. doi:10.1088/1748-9326/aba470.

Cunliffe, A. M., R. E. Brazier, and K. Anderson. 2016. "Ultra-fine Grain Landscape-scale Quantification of Dryland Vegetation Structure with Drone-acquired Structure-from-motion Photogrammetry." *Remote Sensing of Environment* 183: 129–143. doi:10.1016/j.rse.2016.05.019.

Dash, J., and P. J. Curran. 2004. "The MERIS Terrestrial Chlorophyll Index." *International Journal of Remote Sensing* 25 (23): 5403–5413. doi:10.1080/0143116042000274015.

Datt, B. 1999. "Visible/near Infrared Reflectance and Chlorophyll Content in Eucalyptus Leaves." *International Journal of Remote Sensing* 20 (14): 2741–2759. doi:10.1080/014311699211778.

Datt, B. 1998. "Remote Sensing of Chlorophyll A, Chlorophyll B, Chlorophyll A+b, and Total Carotenoid Content in Eucalyptus Leaves." *Remote Sensing of Environment* 66 (2): 111–121. doi:10.1016/S0034-4257(98)00046-7.

Daughtry, C. S. T., C. L. Walthall, M. S. Kim, E. B. De Colstoun, and J. E. McMurtrey Iii. 2000. "Estimating Corn Leaf Chlorophyll Concentration from Leaf and Canopy Reflectance." *Remote Sensing of Environment* 74 (2): 229–239. doi:10.1016/S0034-4257(00)00113-9.

Dinsmore, K. J., J. Drewer, P. E. Levy, C. George, A. Lohila, M. Aurela, and U. M. Skiba. 2017. "Growing Season CH_4 and N_2O Fluxes from a Subarctic Landscape in Northern Finland; from Chamber to Landscape Scale." *Biogeosciences* 14 (4): 799–815. doi:10.5194/bg-14-799-2017.

Duckworth, J. C., M. Kent, and P. M. Ramsay. 2000. "Plant Functional Types: An Alternative to Taxonomic Plant Community Description in Biogeography?." *Progress in Physical Geography* 24 (4): 515–542. doi:10.1191/030913300701542778.

Elvidge, C. D., and Z. Chen. 1995. "Comparison of Broad-band and Narrow-band Red and Near-infrared Vegetation Indices." *Remote Sensing of Environment* 54 (1): 38–48. doi:10.1016/0034-4257(95)00132-K.

Epstein, H. E., M. K. Raynolds, D. A. Walker, U. S. Bhatt, C. J. Tucker, and J. E. Pinzon. 2012. "Dynamics of Aboveground Phytomass of the Circumpolar Arctic Tundra during the past Three Decades." *Environmental Research Letters* 7 (1): 1. doi:10.1088/1748-9326/7/1/015506.

Falcioni, R., T. Moriwaki, M. Pattaro, R. H. Furlanetto, M. R. Nanni, and W. C. Antunes. 2020. "High Resolution Leaf Spectral Signature as a Tool for Foliar Pigment Estimation Displaying

Potential for Species Differentiation." *Journal of Plant Physiology* 249: 153161. doi:10.1016/j.jplph.2020.153161.

Filella, I., and J. Penuelas. 1994. "The Red Edge Position and Shape as Indicators of Plant Chlorophyll Content, Biomass and Hydric Status." *International Journal of Remote Sensing* 15 (7): 1459–1470. doi:10.1080/01431169408954177.

Fraser, R. H., T. C. L. Ian Olthof, and C. Schmitt. 2016. "UAV Photogrammetry for Mapping Vegetation in the low-Arctic." *Arctic Science* 2 (3): 79–102. doi:10.1139/as-2016-0008.

Gamon, J. A., J. Peñuelas, and C. B. Field. 1992. "A Narrow-waveband Spectral Index that Tracks Diurnal Changes in Photosynthetic Efficiency." *Remote Sensing of Environment* 41 (1): 35–44. doi:10.1016/0034-4257(92)90059-S.

Gandia, S., G. Fernández, J. C. García, and J. Moreno. 2004. "Retrieval of Vegetation Biophysical Variables from CHRIS/PROBA Data in the SPARC Campaing." Proceedings of the 2nd CHRIS/Proba Workshop, ESA/ESRIN, Frascati, Italy, April 28–30 (ESA SP-578, July 2004).

Garrity, S. R., U. H. E. Jan, and L. A. Vierling. 2011. "Disentangling the Relationships between Plant Pigments and the Photochemical Reflectance Index Reveals a New Approach for Remote Estimation of Carotenoid Content." *Remote Sensing of Environment* 115 (2): 628–635. doi:10.1016/j.rse.2010.10.007.

Gholizadeh, H., J. A. Gamon, C. J. Helzer, and J. Cavender-Bares. 2020. "Multi-temporal Assessment of Grassland α- and β-diversity Using Hyperspectral Imaging." *Ecological Applications*. doi:10.1002/eap.2145.

Gitelson, A., and M. N. Merzlyak. 1994. "Quantitative Estimation of Chlorophyll-a Using Reflectance Spectra: Experiments with Autumn Chestnut and Maple Leaves." *Journal of Photochemistry and Photobiology, B: Biology* 22 (3): 247–252. doi:10.1016/1011-1344(93)06963-4.

Gitelson, A. A., Y. J. Kaufman, and M. N. Merzlyak. 1996. "Use of a Green Channel in Remote Sensing of Global Vegetation from EOS- MODIS." *Remote Sensing of Environment* 58 (3): 289–298. doi:10.1016/S0034-4257(96)00072-7.

Gitelson, A. A., and M. N. Merzlyak. 1997. "Remote Estimation of Chlorophyll Content in Higher Plant Leaves." *International Journal of Remote Sensing* 18 (12): 2691–2697. doi:10.1080/014311697217558.

Gitelson, A. A., C. Buschmann, and H. K. Lichtenthaler. 1999. "The Chlorophyll Fluorescence Ratio F735/F700 as an Accurate Measure of the Chlorophyll Content in Plants." *Remote Sensing of Environment* 69 (3): 296–302. doi:10.1016/S0034-4257(99)00023-1.

Gitelson, A. A., Y. Gritz †, and M. N. Merzlyak. 2003. "Relationships between Leaf Chlorophyll Content and Spectral Reflectance and Algorithms for Non-destructive Chlorophyll Assessment in Higher Plant Leaves." *Journal of Plant Physiology* 160 (3): 271–282. doi:10.1078/0176-1617-00887.

Greaves, H. E., L. A. Vierling, J. U. H. Eitel, N. T. Boelman, T. S. Magney, C. M. Prager, and K. L. Griffin. 2016. "High-resolution Mapping of Aboveground Shrub Biomass in Arctic Tundra Using Airborne Lidar and Imagery." *Remote Sensing of Environment* 184: 361–373. doi:10.1016/j.rse.2016.07.026.

Greaves, H. E., L. A. Vierling, J. U. H. Eitel, N. T. Boelman, T. S. Magney, C. M. Prager, and K. L. Griffin. 2017. "Applying Terrestrial Lidar for Evaluation and Calibration of Airborne Lidar-derived Shrub Biomass Estimates in Arctic Tundra." *Remote Sensing Letters* 8 (2): 175–184. doi:10.1080/2150704X.2016.1246770.

Grizonnet, M., J. Michel, V. Poughon, J. Inglada, M. Savinaud, and R. Cresson. 2017. "Orfeo ToolBox: Open Source Processing of Remote Sensing Images." *Open Geospatial Data, Software and Standards* 2 (1): 15. doi:10.1186/s40965-017-0031-6.

Guisan, A., S. B. Weiss, and A. D. Weiss. 1999. "GLM versus CCA Spatial Modeling of Plant Species Distribution." *Plant Ecology* 143 (1): 107–122. doi:10.1023/A:1009841519580.

Guyot, G., and F. Baret. 1988. "Utilisation De La Haute Resolution Spectrale Pour Suivre L'etat Des Couverts Vegetaux." Paper presented at the Spectral Signatures of Objects in Remote Sensing, Aussois (Modane), France.

Haboudane, D., J. R. Miller, N. Tremblay, P. J. Zarco-Tejada, and L. Dextraze. 2002. "Integrated Narrow-band Vegetation Indices for Prediction of Crop Chlorophyll Content for Application to Precision Agriculture." *Remote Sensing of Environment* 81 (2): 416–426. doi:10.1016/S0034-4257(02)00018-4.

Halabisky, M., C. Babcock, and L. M. Moskal. 2018. "Harnessing the Temporal Dimension to Improve Object-based Image Analysis Classification of Wetlands." *Remote Sensing* 10 (9): 1467. doi:10.3390/rs10091467.

Hall-Beyer, M. 2017. "Practical Guidelines for Choosing GLCM Textures to Use in Landscape Classification Tasks over a Range of Moderate Spatial Scales." *International Journal of Remote Sensing* 38 (5): 1312–1338. doi:10.1080/01431161.2016.1278314.

Haralick, R. M., I. Dinstein, and K. Shanmugam. 1973. "Textural Features for Image Classification." *IEEE Transactions on Systems, Man and Cybernetics* SMC-3 (6): 610–621. doi:10.1109/TSMC.1973.4309314.

Harris, A., and A. J. Baird. 2019. "Microtopographic Drivers of Vegetation Patterning in Blanket Peatlands Recovering from Erosion." *Ecosystems* 22 (5): 1035–1054. doi:10.1007/s10021-018-0321-6.

Harris, A., R. Charnock, and R. M. Lucas. 2015. "Hyperspectral Remote Sensing of Peatland Floristic Gradients." *Remote Sensing of Environment* 162: 99–111. doi:10.1016/j.rse.2015.01.029.

Harris, A., and J. Dash 2011. "A New Approach for Estimating Northern Peatland Gross Primary Productivity Using A Satellite-sensor-derived Chlorophyll Index." *Journal of Geophysical Research* 116(G4). doi:10.1029/2011jg001662.

Hernández-Clemente, R., R. M. Navarro-Cerrillo, L. Suárez, F. Morales, and P. J. Zarco-Tejada. 2011. "Assessing Structural Effects on PRI for Stress Detection in Conifer Forests." *Remote Sensing of Environment* 115 (9): 2360–2375. doi:10.1016/j.rse.2011.04.036.

Hernández-Clemente, R., R. M. Navarro-Cerrillo, and P. J. Zarco-Tejada. 2012. "Carotenoid Content Estimation in a Heterogeneous Conifer Forest Using Narrow-band

Indices and PROSPECT+DART Simulations." *Remote Sensing of Environment* 127: 298–315. doi:10.1016/j.rse.2012.09.014.

Honkavaara, E., T. Rosnell, R. Oliveira, and A. Tommaselli. 2017. "Band Registration of Tuneable Frame Format Hyperspectral UAV Imagers in Complex Scenes." *ISPRS Journal of Photogrammetry and Remote Sensing* 134: 96–109. doi:10.1016/j.isprsjprs.2017.10.014.

Huete, A. R. 1988. "A Soil-adjusted Vegetation Index (SAVI)." *Remote Sensing of Environment* 25 (3): 295–309. doi:10.1016/0034-4257(88)90106-x.

Hugelius, G., T. Virtanen, D. Kaverin, A. Pastukhov, F. Rivkin, S. Marchenko, V. Romanovsky, and P. Kuhry. 2011. "High-resolution Mapping of Ecosystem Carbon Storage and Potential Effects of Permafrost Thaw in Periglacial Terrain, European Russian Arctic." *Journal of Geophysical Research: Biogeosciences* 116 (3). doi:10.1029/2010JG001606.

Jakob, S., R. Zimmermann, and R. Gloaguen. 2017. "The Need for Accurate Geometric and Radiometric Corrections of Drone-Borne Hyperspectral Data for Mineral Exploration: MEPHySTo—A Toolbox for Pre-Processing Drone-Borne Hyperspectral Data." *Remote Sensing* 9 (1): 88. doi:10.3390/rs9010088.

Jordan, C. F. 1969. "Derivation of Leaf-Area Index from Quality of Light on the Forest Floor." *Ecology* 50 (4): 663–666. doi:10.2307/1936256.

Juutinen, S., T. Virtanen, V. Kondratyev, T. Laurila, M. Linkosalmi, J. Mikola, J. Nyman, A. Räsänen, J.-P. Tuovinen, and M. Aurela. 2017. "Spatial Variation and Seasonal Dynamics of Leaf-area Index in the Arctic Tundra-implications for Linking Ground Observations and Satellite Images." *Environmental Research Letters* 12 (9): 095002. doi:10.1088/1748-9326/aa7f85.

Kalacska, M., G. L. Chmura, O. Lucanus, D. Bérubé, and J. P. Arroyo-Mora. 2017. "Structure from Motion Will Revolutionize Analyses of Tidal Wetland Landscapes." *Remote Sensing of Environment* 199: 14–24. doi:10.1016/j.rse.2017.06.023.

Kalacska, M., M. Lalonde, and T. R. Moore. 2015. "Estimation of Foliar Chlorophyll and Nitrogen Content in an Ombrotrophic Bog from Hyperspectral Data: Scaling from Leaf to Image." *Remote Sensing of Environment* 169: 270–279. doi:10.1016/j.rse.2015.08.012.

Kattenborn, T., F. E. Fassnacht, S. Pierce, J. Lopatin, J. P. Grime, S. Schmidtlein, and J. Paruelo. 2017. "Linking Plant Strategies and Plant Traits Derived by Radiative Transfer Modelling." *Journal of Vegetation Science* 28 (4): 717–727. doi:10.1111/jvs.12525.

Kim, M. S., C. S. T. Daughtry, E. W. Chappelle, J. E. McMurtrey, and C. L. Walthall. 1994. "The Use of High Spectral Resolution Bands for Estimating Absorbed Photosynthetically Active Radiation (A Par)." Paper presented at the Proceedings of the Sixth Symposium on Physical Measurements and Signatures in Remote Sensing, Val D'Isere, France.

Klein, D. R., and C. Bay. 1994. "Resource Partitioning by Mammalian Herbivores in the High Arctic." *Oecologia* 97 (4): 439–450. doi:10.1007/BF00325880.

Kursa, M. B., and W. R. Rudnicki. 2010. "Feature Selection with the Boruta Package." *Journal of Statistical Software* 36 (11): 1–13. doi:10.18637/jss.v036.i11.

Laidler, G. J., and P. Treitz. 2003. "Biophysical Remote Sensing of Arctic Environments." *Progress in Physical Geography* 27 (1): 44–68. doi:10.1191/0309133303pp358ra.

Laine, A. M., L. Mehtätalo, A. Tolvanen, S. Frolking, and E. S. Tuittila. 2019. "Impacts of Drainage, Restoration and Warming on Boreal Wetland Greenhouse Gas Fluxes." *Science of the Total Environment* 647: 169–181. doi:10.1016/j.scitotenv.2018.07.390.

Laitinen, J., S. Rehell, A. Huttunen, T. Tahvanainen, R. Heikkilä, and T. Lindholm. 2007. "Mire Systems in Finland - Special View to Aapa Mires and Their Water-flow Pattern." *Suo* 58 (1): 1–26.

le Maire, G., C. François, and E. Dufrêne. 2004. "Towards Universal Broad Leaf Chlorophyll Indices Using PROSPECT Simulated Database and Hyperspectral Reflectance Measurements." *Remote Sensing of Environment* 89 (1): 1–28. doi:10.1016/j.rse.2003.09.004.

le Maire, G., C. François, K. Soudani, D. Berveiller, J.-Y. Pontailler, N. Bréda, H. Genet, H. Davi, and D. Eric. 2008. "Calibration and Validation of Hyperspectral Indices for the Estimation of Broadleaved Forest Leaf Chlorophyll Content, Leaf Mass per Area, Leaf Area Index and Leaf Canopy Biomass." *Remote Sensing of Environment* 112 (10): 3846–3864. doi:10.1016/j.rse.2008.06.005.

Lehmann, J. R. K., W. Münchberger, C. Knoth, C. Blodau, F. Nieberding, T. Prinz, V. A. Pancotto, and T. Kleinebecker. 2016. "High-resolution Classification of South Patagonian Peat Bog Microforms Reveals Potential Gaps in Up-scaled CH_4 Fluxes by Use of Unmanned Aerial System (UAS) and CIR Imagery." *Remote Sensing* 8 (3): 173. doi:10.3390/rs8030173.

Lehnert, L. W., H. Meyer, W. A. Obermeier, B. Silva, B. Regeling, and J. Bendix. 2019. "Hyperspectral Data Analysis in R: The Hsdar Package." *Journal of Statistical Software* 89 (12): 1–23. doi:10.18637/jss.v089.i12.

Li, B., X. Xiangming, L. Zhang, J. Han, C. Bian, L. Guangcun, J. Liu, and L. Jin. 2020. "Above-ground Biomass Estimation and Yield Prediction in Potato by Using UAV-based RGB and Hyperspectral Imaging." *ISPRS Journal of Photogrammetry and Remote Sensing* 162: 161–172. doi:10.1016/j.isprsjprs.2020.02.013.

Liaw, A., and M. Wiener. 2002. "Classification and Regression by randomForest." *R News* 2 (3): 18–22.

Luo, S., C. Wang, X. Xi, H. Zeng, D. Li, S. Xia, and P. Wang. 2016. "Fusion of Airborne Discrete-return LiDAR and Hyperspectral Data for Land Cover Classification." *Remote Sensing* 8 (1). doi:10.3390/rs8010003.

Maccioni, A., G. Agati, and P. Mazzinghi. 2001. "New Vegetation Indices for Remote Measurement of Chlorophylls Based on Leaf Directional Reflectance Spectra." *Journal of Photochemistry and Photobiology B: Biology* 61 (1–2): 52–61. doi:10.1016/S1011-1344(01)00145-2.

McFeeters, S. K. 1996. "The Use of the Normalized Difference Water Index (NDWI) in the Delineation of Open Water Features." *International Journal of Remote Sensing* 17 (7): 1425–1432. doi:10.1080/01431169608948714.

McMurtrey, J. E., E. W. Chappelle, M. S. Kim, J. J. Meisinger, and L. A. Corp. 1994. "Distinguishing Nitrogen Fertilization Levels

in Field Corn (Zea Mays L.) With Actively Induced Fluorescence and Passive Reflectance Measurements." *Remote Sensing of Environment* 47 (1): 36–44. doi:10.1016/0034-4257(94)90125-2.

Metzger, C., P. E. Jansson, A. Lohila, M. Aurela, T. Eickenscheidt, L. Belelli-Marchesini, K. J. Dinsmore, J. Drewer, J. Van Huissteden, and M. Drösler. 2015. "CO2 Fluxes and Ecosystem Dynamics at Five European Treeless Peatlands-merging Data and Process Oriented Modeling." *Biogeosciences* 12 (1): 125–146. doi:10.5194/bg-12-125-2015.

Michez, A., S. Bauwens, Y. Brostaux, M. P. Hiel, S. Garré, P. Lejeune, and B. Dumont. 2018. "How Far Can Consumer-grade UAV RGB Imagery Describe Crop Production? A 3D and Multitemporal Modeling Approach Applied to Zea Mays." *Remote Sensing* 10 (11): 1798. doi:10.3390/rs10111798.

Middleton, M., P. Närhi, H. Arkimaa, E. Hyvönen, V. Kuosmanen, P. Treitz, and R. Sutinen. 2012. "Ordination and Hyperspectral Remote Sensing Approach to Classify Peatland Biotopes along Soil Moisture and Fertility Gradients." *Remote Sensing of Environment* 124: 596–609. doi:10.1016/j.rse.2012.06.010.

Mishra, V. N., R. Prasad, P. K. Rai, A. K. Vishwakarma, and A. Arora. 2018. "Performance Evaluation of Textural Features in Improving Land Use/land Cover Classification Accuracy of Heterogeneous Landscape Using Multi-sensor Remote Sensing Data." *Earth Science Informatics*. doi:10.1007/s12145-018-0369-z.

Moore, P. A., M. C. Lukenbach, D. K. Thompson, N. Kettridge, G. Granath, and J. M. Waddington. 2019. "Assessing the Peatland Hummock–hollow Classification Framework Using High-resolution Elevation Models: Implications for Appropriate Complexity Ecosystem Modeling." *Biogeosciences* 16 (18): 3491–3506. doi:10.5194/bg-16-3491-2019.

Myers-Smith, I. H., S. C. Elmendorf, P. S. A. Beck, M. Wilmking, M. Hallinger, D. Blok, K. D. Tape, et al.. 2015. "Climate Sensitivity of Shrub Growth across the Tundra Biome." *Nature Climate Change* 5 (9): 887-+. doi:10.1038/nclimate2697.

Oppelt, N., and W. Mauser. 2004. "Hyperspectral Monitoring of Physiological Parameters of Wheat during a Vegetation Period Using AVIS Data." *International Journal of Remote Sensing* 25 (1): 145–159. doi:10.1080/0143116031000115300.

Palace, M., C. Herrick, J. DelGreco, D. Finnell, A. J. Garnello, C. McCalley, K. McArthur, F. Sullivan, and R. K. Varner. 2018. "Determining Subarctic Peatland Vegetation Using an Unmanned Aerial System (UAS)." *Remote Sensing* 10 (9): 1498. doi:10.3390/rs10091498.

Planet Team. "Planet Application Program Interface: In Space for Life on Earth." https://api.planet.com

Poley, L. G., and G. J. McDermid. 2020. "A Systematic Review of the Factors Influencing the Estimation of Vegetation Aboveground Biomass Using Unmanned Aerial Systems." *Remote Sensing* 12 (7): 1052. doi:10.3390/rs12071052.

Qi, J., A. Chehbouni, A. R. Huete, Y. H. Kerr, and S. Sorooshian. 1994. "A Modified Soil Adjusted Vegetation Index." *Remote Sensing of Environment* 48 (2): 119–126. doi:10.1016/0034-4257(94)90134-1.

R Core Team. 2018. *R: A Language and Environment for Statistical Computing*. Vienna, Austria: R Foundation for Statistical Computing.

Räsänen, A., S. Juutinen, M. Aurela, and T. Virtanen. 2019. "Predicting Aboveground Biomass in Arctic Landscapes Using Very High Spatial Resolution Satellite Imagery and Field Sampling." *International Journal of Remote Sensing* 40 (3): 1175–1199. doi:10.1080/01431161.2018.1524176.

Räsänen, A., and T. Virtanen. 2019. "Data and Resolution Requirements in Mapping Vegetation in Spatially Heterogeneous Landscapes." *Remote Sensing of Environment* 230: 111207. doi:10.1016/j.rse.2019.05.026.

Räsänen, A., M. Aurela, S. Juutinen, T. Kumpula, A. Lohila, T. Penttilä, and T. Virtanen. 2020. "Detecting Northern Peatland Vegetation Patterns at Ultra-high Spatial Resolution." *Remote Sensing in Ecology and Conservation*. doi:10.1002/rse2.140.

Rondeaux, G., M. Steven, and F. Baret. 1996. "Optimization of Soil-adjusted Vegetation Indices." *Remote Sensing of Environment* 55 (2): 95–107. doi:10.1016/0034-4257(95)00186-7.

Roujean, J.-L., and F.-M. Breon. 1995. "Estimating PAR Absorbed by Vegetation from Bidirectional Reflectance Measurements." *Remote Sensing of Environment* 51 (3): 375–384. doi:10.1016/0034-4257(94)00114-3.

Rouse, J. W., Jr., R. H. Haas, J. A. Schell, and D. W. Deering. 1974. "Monitoring Vegetation Systems in the Great Plains with ERTS." In *Third Earth Resources Technology Satellite-1 Symposium*, 309–317. Washington, DC: NASA.

Sankey, T. T., J. McVay, T. L. Swetnam, M. P. McClaran, P. Heilman, and M. Nichols. 2018. "UAV Hyperspectral and Lidar Data and Their Fusion for Arid and Semi-arid Land Vegetation Monitoring." *Remote Sensing in Ecology and Conservation* 4 (1): 20–33. doi:10.1002/rse2.44.

Schmidtlein, S., H. Feilhauer, H. Bruelheide, and D. Rocchini. 2012. "Mapping Plant Strategy Types Using Remote Sensing." *Journal of Vegetation Science* 23 (3): 395–405. doi:10.1111/j.1654-1103.2011.01370.x.

Smith, R. C. G., J. Adams, D. J. Stephens, and P. T. Hick. 1995. "Forecasting Wheat Yield in a Mediterranean-type Environment from the NOAA Satellite." *Australian Journal of Agricultural Research* 46 (1): 113–125. doi:10.1071/AR9950113.

Treat, C. C., M. E. Marushchak, C. Voigt, Y. Zhang, Z. Tan, Q. Zhuang, T. A. Virtanen, et al.. 2018. "Tundra Landscape Heterogeneity, Not Interannual Variability, Controls the Decadal Regional Carbon Balance in the Western Russian Arctic." *Global Change Biology* 24 (11): 5188–5204. doi:10.1111/gcb.14421.

Tuovinen, J. P., M. Aurela, J. Hatakka, A. Räsänen, T. Virtanen, J. Mikola, V. Ivakhov, V. Kondratyev, and T. Laurila. 2019. "Interpreting Eddy Covariance Data from Heterogeneous Siberian Tundra: Land-cover-specific Methane Fluxes and

Spatial Representativeness." *Biogeosciences* 16 (2): 255–274. doi:10.5194/bg-16-255-2019.

Turner, D. J., Z. Malenovsky, A. Lucieer, J. D. Turnbull, and S. A. Robinson. 2019. "Optimizing Spectral and Spatial Resolutions of Unmanned Aerial System Imaging Sensors for Monitoring Antarctic Vegetation." *IEEE Journal of Selected Topics in Applied Earth Observations and Remote Sensing* 12 (10): 3813–3825. doi:10.1109/JSTARS.2019.2938544.

Ustin, S. L., and J. A. Gamon. 2010. "Remote Sensing of Plant Functional Types." *New Phytologist* 186 (4): 795–816. doi:10.1111/j.1469-8137.2010.03284.x.

van der Wal, R., and A. Stien. 2014. "High-arctic Plants like It Hot: A Long-term Investigation of Between-year Variability in Plant Biomass." *Ecology* 95 (12): 3414–3427. doi:10.1890/14-0533.1.

Vincini, M., E. Frazzi, and P. D'Alessio. 2006. "Angular Dependence of Maize and Sugar Beet VIs from Directional CHRIS/PROBA Data." In *Fourth ESA CHRIS PROBA Workshop*, 19–21. Frascati, Italy.

Virtanen, T., and M. Ek. 2014. "The Fragmented Nature of Tundra Landscape." *International Journal of Applied Earth Observation and Geoinformation* 27: 4–12. doi:10.1016/j.jag.2013.05.010.

Vogelmann, J. E., B. N. Rock, and D. M. Moss. 1993. "Red Edge Spectral Measurements from Sugar Maple Leaves." *International Journal of Remote Sensing* 14 (8): 1563–1575. doi:10.1080/01431169308953986.

Walker, D. A., H. E. Epstein, G. J. Jia, A. Balser, C. Copass, E. J. Edwards, W. A. Gould, et al.. 2003. "Phytomass, LAI, and NDVI in Northern Alaska: Relationships to Summer Warmth, Soil pH, Plant Functional Types, and Extrapolation to the Circumpolar Arctic." *Journal of Geophysical Research-Atmospheres* 108 (D2). doi:10.1029/2001jd000986.

Wallace, L., A. Lucieer, Z. Malenovský, D. Turner, and V. Petr. 2016. "Assessment of Forest Structure Using Two UAV Techniques: A Comparison of Airborne Laser Scanning and Structure from Motion (Sfm) Point Clouds." *Forests* 7 (3): 62. doi:10.3390/f7030062.

Wang, F., F. Wang, Y. Zhang, J. Hu, J. Huang, and J. Xie. 2019. "Rice Yield Estimation Using Parcel-level Relative Spectral Variables from Uav-based Hyperspectral Imagery." *Frontiers in Plant Science* 10. doi:10.3389/fpls.2019.00453.

Wang, R., J. A. Gamon, J. Cavender-Bares, P. A. Townsend, and A. I. Zygielbaum. 2018. "The Spatial Sensitivity of the Spectral Diversity–biodiversity Relationship: An Experimental Test in a Prairie Grassland." *Ecological Applications* 28 (2): 541–556. doi:10.1002/eap.1669.

Wilson, D., J. Alm, T. Riutta, J. Laine, K. A. Byrne, E. P. Farrell, and E.-S. Tuittila. 2007. "A High Resolution Green Area Index for Modelling the Seasonal Dynamics of CO2 Exchange in Peatland Vascular Plant Communities." *Plant Ecology* 190 (1): 37–51. doi:10.1007/s11258-006-9189-1.

Wu, C., Z. Niu, Q. Tang, and W. Huang. 2008. "Estimating Chlorophyll Content from Hyperspectral Vegetation Indices: Modeling and Validation." *Agricultural and Forest Meteorology* 148 (8–9): 1230–1241. doi:10.1016/j.agrformet.2008.03.005.

Wu, W. 2014. "The Generalized Difference Vegetation Index (GDVI) for Dryland Characterization." *Remote Sensing* 6 (2): 1211–1233. doi:10.3390/rs6021211.

Yu, Q., H. Epstein, R. Engstrom, and D. Walker. 2017. "Circumpolar Arctic Tundra Biomass and Productivity Dynamics in Response to Projected Climate Change and Herbivory." *Global Change Biology* 23 (9): 3895–3907. doi:10.1111/gcb.13632.

Yue, J., G. Yang, C. Li, Z. Li, Y. Wang, H. Feng, and B. Xu. 2017. "Estimation of Winter Wheat Above-ground Biomass Using Unmanned Aerial Vehicle-based Snapshot Hyperspectral Sensor and Crop Height Improved Models." *Remote Sensing* 9 (7). doi:10.3390/rs9070708.

Zarco-Tejada, P. J., V. González-Dugo, L. E. Williams, L. Suárez, J. A. J. Berni, D. Goldhamer, and E. Fereres. 2013. "A PRI-based Water Stress Index Combining Structural and Chlorophyll Effects: Assessment Using Diurnal Narrow-band Airborne Imagery and the CWSI Thermal Index." *Remote Sensing of Environment* 138: 38–50. doi:10.1016/j.rse.2013.07.024.

Zarco-Tejada, P. J., and J. R. Miller. 1999. "Land Cover Mapping at BOREAS Using Red Edge Spectral Parameters from CASI Imagery." *Journal of Geophysical Research: Atmospheres* 104 (D22): 27921–27933. doi:10.1029/1999JD900161.

Zarco-Tejada, P. J., J. C. Pushnik, S. Dobrowski, and S. L. Ustin. 2003. "Steady-state Chlorophyll a Fluorescence Detection from Canopy Derivative Reflectance and Double-peak Red-edge Effects." *Remote Sensing of Environment* 84 (2): 283–294. doi:10.1016/S0034-4257(02)00113-X.